The Astrophysical Journal, 631:947–963, 2005 October 1

A DETAILED STUDY OF MOLECULAR CLOUDS TOWARD THE TeV GAMMA-RAY SUPERNOVA REMNANT G347.3−0.5

Y. Moriguchi, K. Tamura, Y. Tawara, H. Sasago, K. Yamaoka, T. Onishi, and Y. Fukui
Department of Astrophysics, Nagoya University, Chikusa-ku, Nagoya 464-8602, Japan; mori@a.phys.nagoya-u.ac.jp
Received 2005 January 18; accepted 2005 June 11

ABSTRACT

The supernova remnant G347.3−0.5 (J1713.7−3946) is known as one of the unique SNRs that emit TeV γ-rays, as well as nonthermal X-rays. We present a detailed study of molecular gas toward this SNR obtained with the 4 m millimeter and submillimeter telescope NANTEN at an angular resolution of 2′.6. This study has revealed that several intensity peaks and the overall distribution of the molecular gas with radial velocities from −12 to −3 km s^{-1} show a remarkably good correlation with the X-ray features, strongly supporting the recently derived kinematic distance around 1 kpc, as opposed to the 6 kpc previously claimed. In addition, we show that absorption of X-rays is caused by local molecular gas at softer X-ray bands. Subsequent measurements of the submillimeter $J = 3$–2 transition of CO made with the ASTE 10 m and CSO 10.4 m submillimeter telescopes toward three of the molecular intensity peaks have revealed higher excitation conditions, most likely higher temperatures above ∼30 K, in contrast to the typical gas temperature, 10 K, in low-mass dark clouds. This temperature rise is most likely caused by enhanced heating by the high-energy events in the SNR, where possible mechanisms include heating by X-rays, γ-rays, and/or cosmic-ray protons, although we admit that additional radiative heating by young protostars embedded may be working as well. In one of the CO peaks, we have confirmed the presence of broad molecular wings of ∼20 km s^{-1} velocity extent in the CO $J = 3$–2 transition. Two alternative interpretations for the wings are presented; one is shock acceleration by the blast wave, and the other is molecular outflow driven by an embedded protostar. The SNR evolution is well explained as the free expansion phase based on the distance of 1 kpc. The molecular data set should be valuable for making a further detailed comparison with the γ-ray and X-ray distributions in order to examine the cosmic-ray acceleration quantitatively.

Subject headings: cosmic rays — ISM: individual (SNR J1713.37−3946) — ISM: kinematics and dynamics — supernova remnants

Online material: color figures

1. INTRODUCTION

Supernovae are generally thought to be the most energetic events in the Galactic disk, and supernova remnants (SNRs) have profound effects on the dynamics and physical/chemical processes in interstellar space through direct interactions with the surroundings, providing a unique laboratory for testing high-energy processes related to strong shocks. Because of the large energy release of 10^{51} ergs, SNRs have also been considered as the origin of Galactic cosmic rays (e.g., Shklovskii 1953; Hayakawa 1956; Ginzburg 1957). Cosmic rays themselves have brought crucial information on elementary particles and in addition play a crucial role in the evolution of the interstellar medium mainly via heating and ionization, although the detailed physics of particle acceleration in SNRs remains unclear. It is therefore one of the key issues in astrophysics to elucidate the interaction of SNRs with their ambient matter and the probable production of cosmic rays therein.

Observations of interstellar gas have revealed the interactions between SNRs and their surroundings under various physical conditions including ionized hot gas, neutral atomic gas, and dense molecular gas (e.g., Rho et al. 1994 [optical and X-ray], Koo & Heiles 1991 [H I], van Dishoeck et al. 1993 [molecular line]). In particular, millimeter and submillimeter wave observations of dense molecular gas have proved to be a powerful probe of the shocked gas and the interactions; broad wings of several ×10 km s^{-1} accelerated by the shocks are observed in several SNRs in the millimeter and submillimeter spectra of interstellar CO and other molecules (e.g., W44, Seta et al. 1998; W28, Arikawa et al. 1999; IC 443, White et al. 1987). Note also that observations of molecular gas are extremely useful in constraining the kinematic distance of SNRs owing to the better angular resolutions of millimeter-wave telescopes and the intrinsic smaller velocity dispersions of the molecular gas compared to atomic gas.

On the other hand, observational indications for the acceleration of high-energy particles in SNRs have been quite poor particularly for cosmic-ray protons. Cosmic rays consist of protons as the major constituent, as well as of other minor constituents including electrons and heavier atomic nuclei. For years, observational indications for the cosmic-ray particles in SNRs were available only for the electrons that emit synchrotron radiation in the radio band. The highest energy of such electrons is, however, on the order of MeV, much below the highest energy of Galactic cosmic rays around 10^{15} eV. The detection of nonthermal X-ray emission from the shell-type SNR SN 1006 provided evidence for such very high energy electrons (e.g., Koyama et al. 1995). Considering the very short lifetime of such high-energy electrons, the site of their production is definitely constrained to the SNR itself. We are, however, still lacking in understanding of the origin of the major constituent, cosmic-ray protons, as there is not yet clear evidence for proton acceleration in SNRs.

Two shell-type remnants with nonthermal-dominant X-ray spectra have been identified subsequently; they are G347.3−0.5 (Koyama et al. 1997; Slane et al. 1999) and G266.2−1.2 (Slane

et al. 2001). G347.3−0.5 (RX J1713.7−3946) was first discovered in the *ROSAT* (*Röntgensatellit*) All-Sky Survey by Pfeffermann & Aschenbach (1996). Later, *ASCA* (*Advanced Satellite for Cosmology and Astrophysics*) observations revealed that the X-ray emission from the remnant is predominantly nonthermal (Koyama et al. 1997; Slane et al. 1999). The remnant is $\sim 1^\circ$ in diameter and appears to be of a shell-type morphology with the brightest emission in the western region (we use equatorial coordinates to identify directions in the sky throughout this paper). Uchiyama et al. (2003) showed that the synchrotron cutoff energy is unusually high beyond 10 keV, corresponding to 10^{14} eV as the highest particle energies. G347.3−0.5 was also detected at the TeV γ-ray range with the CANGAROO telescope (Muraishi et al. 2000; Enomoto et al. 2002), and models of broadband emission point to IC scattering as the origin of the TeV γ-ray photons (Muraishi et al. 2000; Ellison et al. 2001). More recently, follow-up TeV γ-ray observations have led to a different conclusion, suggesting pion decay as the source of energetic photons (Enomoto et al. 2002), but the nature of this emission is still uncertain (see Butt et al. 2002; Reimer & Pohl 2002; Aharonian et al. 2004).

The SNR is located at $l \sim 347^\circ$, toward the direction of the central part of the Galaxy, a very crowded region with various Galactic objects in the line of sight. This makes it particularly confusing and uncertain to identify physically associated objects, and accordingly, the distance was rather poorly determined at best. The determination of the distance is crucial in all interpretations of observations. Originally, Pfeffermann & Aschenbach (1996) adopted a distance to the SNR of $\sim$1 kpc based on the estimate of the column density derived from the spectral analysis of the *ASCA* data (see also Koyama et al. 1997). Later, the possible association of a molecular cloud (later referred to as "cloud A") was used to derive a distance of 6.3 ± 0.4 kpc from observations of the 2.6 mm CO ($J = 1$–0) line emission at $9'$ resolution by Slane et al. (1999). In their discussion, these authors argued that an enhanced value of the CO ($J = 2$–1)/($J = 1$–0) line ratio in cloud A indicates the physical interaction with the SNR shock (see also Butt et al. 2001). This estimate, $\sim$6 kpc, was often used in subsequent studies of the physical properties of G347.3−0.5 (e.g., Lazendic et al. 2004; Pannuti et al. 2003; Cassam-Chenai et al. 2004b).

Most recently, Fukui et al. (2003, hereafter Paper I) performed new CO observations at 2.6 mm wavelength with NANTEN, a 4 m millimeter and submillimeter telescope located at Las Campanas Observatory in Chile. These new observations have a resolution of $2'.6$, a factor of 3.4 better than that of the CO data used by Slane et al. (1999). The authors discovered molecular gas at a distance of $\sim$1 kpc that shows a holelike distribution having a striking correlation with the X-ray image of G347.3−0.5, in addition to the presence of a broad CO line in one of the CO peaks that likely represents dynamical interaction between the SNR shock and the ambient molecular gas. They also find that cloud A shows worse spatial contact with the edge of the SNR than in the lower resolution CO data. In addition, Koo (2003), Koo et al. (2004), and Cassam-Chenai et al. (2004a) derive a similar distance $\sim$1 kpc by analyzing and comparing it with X-ray absorption. Most recently, the HESS collaboration made a better resolution image of TeV γ-rays and has supported the interaction of the SNR with the CO clouds at $\sim$1 kpc (Aharonian et al. 2004).

Subsequent to Paper I, we present in this paper a detailed analysis of the CO distributions and the physical properties of molecular clouds associated with G347.3−0.5. We present the observations in § 2 and the results of the observations in § 3. We discuss the distance, the evolutionary phase, and the surrounding environments of the SNR in § 4 and give conclusions in § 5.

2. OBSERVATIONS

Observations were made in the ^{12}CO ($J = 1$–0) line by using a 4 m millimeter/submillimeter telescope of Nagoya University, NANTEN, at Las Campanas Observatory, Chile. The telescope had a half-power beamwidth (HPBW) of $2'.6$ at a frequency of 115 GHz and was equipped with a 4 K cryogenically cooled Nb superconductor-insulator-superconductor (SIS) mixer receiver (Ogawa et al. 1990) that provided a typical system temperature of $\sim$250 K in the single-side band, including the atmosphere toward the zenith. NANTEN was equipped with two acousto-optical spectrometers (AOSs) with 2048 channels. The total bandwidth and the effective resolution were 250 MHz and 250 kHz for wideband mode, corresponding to a velocity coverage of 600 km s^{-1} and a velocity resolution of 0.65 km s^{-1}, respectively. The present observations used the wideband mode. The data are part of the NANTEN Galactic Plane Survey. The survey carried out from 1999 to 2003 observed about 1.1 million points in total, covering a Galactic longitude range of 240° (from $l = 180^\circ$ to 60°) and Galactic latitude coverage of 10°–20° at $4'$–$8'$ (partly $2'$) grid spacing. The grid spacing for the longitude coverage is basically $4'$ for $|b| \leq 5^\circ$ and $8'$ for $|b| \geq 5^\circ$ (see Matsunaga et al. 2001).[1]

After the $4'$ grid unbiased survey, we carried out a sensitive $2'$ grid survey, by covering the whole area of G347.3−0.5 in 2003 April. An area of $\sim$1.91 deg^2 in the region of $346^\circ.7 \leq l \leq 348^\circ.0$ and $-1^\circ.2 \leq b \leq 0^\circ.2$ was mapped. The integration time was typically $\sim$10 s per point, resulting in typical rms noise fluctuations of 0.2–0.3 K at a velocity resolution of 0.65 km s^{-1}. In total, 1720 positions were observed. For the intensity calibration, the room-temperature chopper wheel method was employed, and the absolute intensity was calibrated by observing Orion KL [$\alpha(1950) = 5^{\rm h}32^{\rm m}47^{\rm s}.0$, $\delta(1950) = -5^\circ 24' 21''$] and ρ Oph East [$\alpha(1950) = 16^{\rm h}29^{\rm m}20^{\rm s}.9$, $\delta(1950) = -24^\circ 22' 13''$] every few hours. We assumed the absolute radiation temperatures, T_R^*, of Orion KL and ρ Oph East to be 65 and 15 K, respectively.

Following the NANTEN survey, we have carried out a ^{12}CO ($J = 3$–2) one-point observation toward one of the strong ^{12}CO ($J = 1$–0) peaks identified with NANTEN, peak C discussed in Paper I, using the 10.4 m telescope at the Caltech Submillimeter Observatory (CSO) in 2004 April. CSO is installed at the summit of Mount Mauna Kea at an altitude of 4000 m. The observed position is $(l,\ b) = (347^\circ.07,\ -0^\circ.400)$, and the beam size at the ^{12}CO ($J = 3$–2) line was $22''$. CSO was equipped with four AOS's with different bandwidths, 50 MHz, 500 MHz (two), and 1.5 GHz. The number of channels is 2048 for 1.5 GHz and 500 MHz and 1024 for 50 MHz. We used two of these AOSs, the 1.5 GHz and 50 MHz. The effective frequency resolutions were 700 kHz for the 1.5 GHz AOS and 48 kHz for the 50 MHz one. The velocity coverage and resolution were 1200 and 0.61 km s^{-1} for 1.5 GHz and 40 and 0.04 km s^{-1} for 50 MHz, respectively. The system temperature for the 1.5 GHz was $\sim$1200 K for an elevation angle of $\sim 26^\circ$ in the double-side band including the atmosphere. The total integration time is 120 s, and the rms noise temperature per channel is 0.25 K for 1.5 GHz and 0.55 K for 50 MHz. We adopted a beam efficiency $\sim$75% for 345 GHz, the recommended value calculated by past observations of planets.

After that, we carried out a high-resolution extensive ^{12}CO ($J = 3$–2) survey toward G347.3−0.5 using the Atacama

[1] See also the NANTEN2 special issue of PASJ (53 [6] [2001]).

Submillimeter Telescope Experiment (ASTE) 10 m submillimeter telescope of NAOJ (National Astronomical Observatory Japan; Ezawa et al. 2004) located at the site of the Atacama desert in Chile, with an altitude of 4800 m, in 2004 November. The beam size at the ^{12}CO ($J = 3-2$) line was 23″. We have observed the three regions containing the CO peaks selected from Paper I with a grid spacing of 30″ (partially 1′), including 780 observed points in total. ASTE was equipped with four digital back end systems (autocorrelators) with 2048 channels, and we could select either of the two observational modes (wideband or narrowband). The total bandwidths of the wideband and narrowband modes were 512 and 128 MHz, corresponding to effective velocity coverages of 450 and 110 km s^{-1}, respectively. The effective resolutions were 500 and 125 kHz, corresponding to velocity resolutions of 0.43 and 0.12 km s^{-1}, respectively. We used the wideband mode. The system temperature was 300–400 K for an elevation angle of ∼40°–70° in the double-side band including the atmosphere. Total integration time per point is 30 s, and the rms noise temperature per channel is 0.4–0.9 K, respectively. The beam efficiency was ∼50%–60% for 345 GHz in the daytime. For system check and absolute intensity calibration, M17 SW [$\alpha(1950) = 18^h17^m30\overset{s}{.}0$, $\delta(1950) = -16°13'6''$] was observed every day.

3. RESULTS

3.1. *Large-Scale* CO *Distribution*

Figure 1*a* shows a CO map covering from $l = 343°$ to 352° taken with NANTEN as part of the Galactic plane CO survey (Y. Fukui et al. 2005, in preparation) superposed on the *ROSAT* X-ray boundary of SNR G347.3−0.5. The SNR happens to be located toward a hole in the integrated CO intensity. Figure 1*b* shows a velocity-longitude diagram in the same longitude range as Figure 1*a* for a velocity (=radial velocity with respect to the local standard of rest [$V_{\rm LSR}$]) range from −150 to 20 km s^{-1}. The velocity range of the molecular gas argued to be interacting with the SNR is close to ∼0 km s^{-1}, from −12 to −3 km s^{-1} (Paper I). It is seen that the lower negative velocity edge at $V_{\rm LSR} \sim 0$ to −10 km s^{-1} of the Sagittarius arm exhibits an intensity depression at $l \sim 347°$–348°. This corresponds to a cavity-like CO distribution delineating the SNR G347.3−0.5 in Paper I, having a size similar to that of the SNR. More significant is a hole in the CO emission at $V_{\rm LSR} \sim -10$ to ∼−35 km s^{-1} in the same longitude range of $l \sim 347°$–348°, associated with the Sagittarius arm. This hole corresponds to a molecular supershell named SG 347.3-0.0-21 at a distance of ∼3 kpc (Matsunaga et al. 2001), which is likely due to multiple supernova/stellar winds from OB stars. This chance coincidence with the supershell in the line of sight causes the apparent CO depression toward G347.3−0.5 in Figure 1*a*, while the size of the supershell, ∼1°.5, is much larger than that of G347.3−0.5, and they are not likely physically connected. Another feature of past concern is cloud A located at $l \sim 348°$ and $V_{\rm LSR} \sim -90$ km s^{-1}, which was ascribed to be associated with the SNR G347.3−0.5 by Slane et al. (1999). This cloud is rather isolated on the far side of the Norma arm.

3.2. CO *Clouds toward the SNR: Coarse Velocity Channel Maps*

In Figure 2, we present a montage of CO velocity channel maps taken every 10 km s^{-1} from $V_{\rm LSR} = -160$ to 20 km s^{-1}. The directions seen from the center of the SNR in equatorial coordinates are denoted in Figure 2*a*, such as N (north), NE (northeast), and so on. The central position is indicated by the cross, where we adopt $(l,\ b) = (347\overset{\circ}{.}3,\ -0\overset{\circ}{.}5)$, the cataloged position originally given in Pfeffermann & Aschenbach (1996).

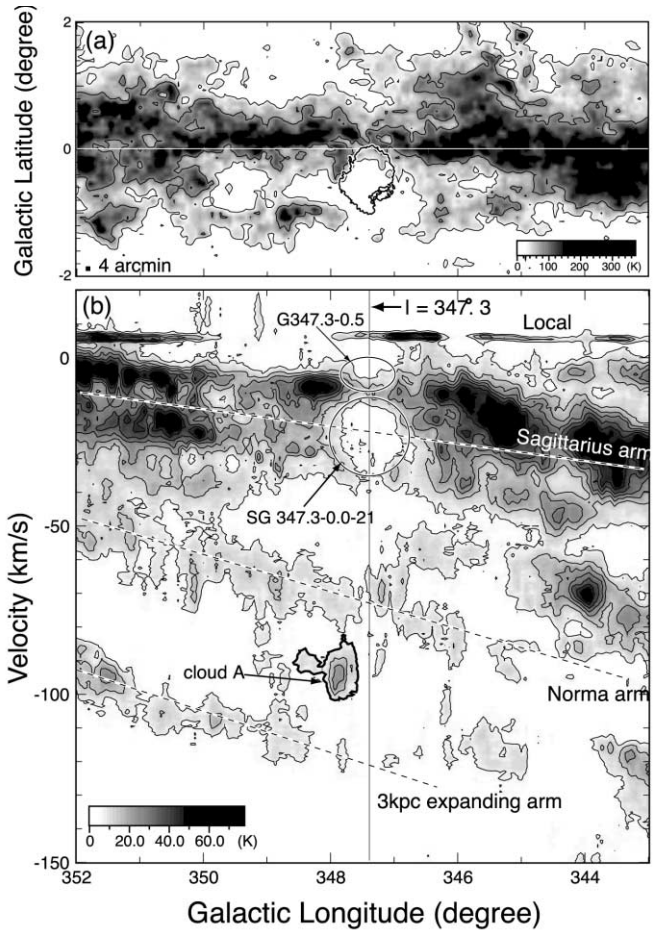

FIG. 1.—(*a*) Large area distribution of ^{12}CO ($J = 1-0$) integrated intensity taken from NANTEN Galactic plane CO survey (Y. Fukui et al. 2005, in preparation; see also Matsunaga et al. 2001). The grid spacing is 4′ with a 2′.6 beam. The lowest contour level and the contour interval are 30 and 80 K km s^{-1} in T_R^*, respectively. The X-ray boundary of G347.3−0.5 (Pfeffermann & Aschenbach 1996) is indicated by a thick line. (*b*) Galactic longitude-velocity map of ^{12}CO ($J = 1-0$) in the same region as (*a*). The integrated range in Galactic latitude is from −1° to 1°. Both the lowest contour level and interval are 7 K. Approximate positions of the Sagittarius arm, Norma arm, and 3 kpc expanding arm are indicated by dashed lines. The position of $l = 347\overset{\circ}{.}3$ is denoted by a solid line. The SNR G347.3−0.5 and the supershell SG 347.3-0.0-21 (Matsunaga et al. 2001) are indicated by a solid ellipse and a circle, respectively. The boundary of cloud A (Slane et al. 1999) is denoted by a thick solid line. [*See the electronic edition of the Journal for a color version of this figure.*]

The kinematic distance corresponding to the velocity centroid at each panel is indicated as calculated by using the Galactic rotation curve model (Brand & Blitz 1993). The outer boundary of the *ROSAT* X-ray image is superposed in each panel for reference. At various velocities, the SNR appears to be in contact with CO features as naturally expected in the direction of the Galactic center, but most of the apparent coincidence must be fortuitous.

At $V_{\rm LSR} \sim -160$ to −110 km s^{-1} (Figs. 2*a*–2*e*) the association of CO with the SNR is not obvious. At −100 to −90 km s^{-1} (Fig. 2*g*), a CO cloud toward $(l,\ b) = (347\overset{\circ}{.}9,\ -0\overset{\circ}{.}3)$ appears close to the boundary of the SNR, which is cloud A. The present data taken at a higher angular resolution than that of Slane et al. (1999) show that the western side of cloud A is not delineating the SNR boundary very well compared to the lower resolution data at 9′, particularly at a latitude range greater than $-0\overset{\circ}{.}3$. Another CO

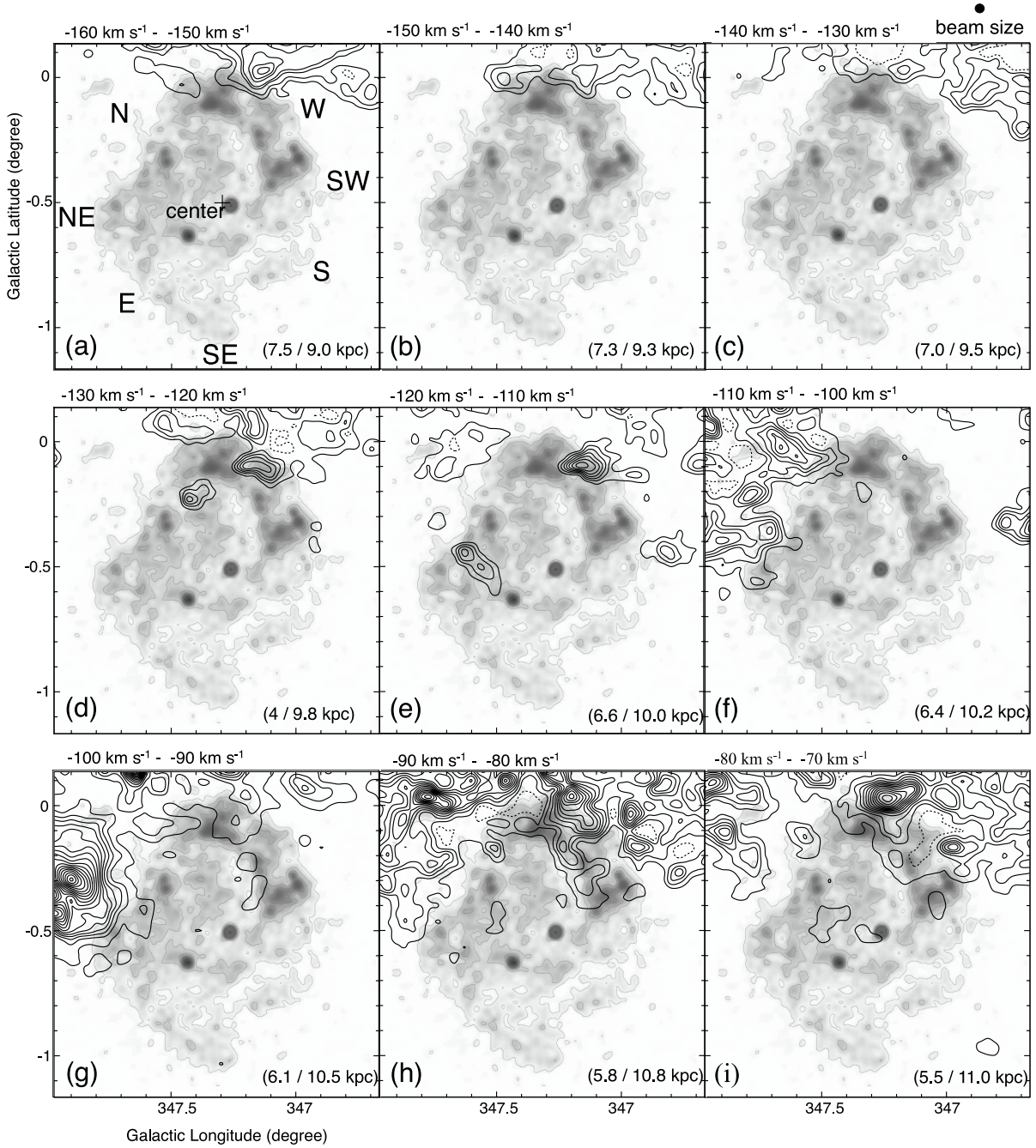

FIG. 2.—^{12}CO ($J = 1$–0) channel maps (*black contours*) superposed with the X-ray image (*gray scale and contours*) by the *ROSAT* PSPC X-Ray Survey (Slane et al. 1999; from *ROSAT* archive database). Each panel shows a CO intensity map integrated over the velocity range from -160 to 20 km s^{-1} every 10 km s^{-1}. The minimum contour level and contour interval are 4 K km s^{-1} in all of the panels except (*g*), (*i*), (*j*), and (*o*). The minimum contour level is 4 K km s^{-1} and the contour interval is 8 K km s^{-1} in (*g*), (*i*), and (*j*). In (*o*), the contour levels are 4, 8, 12, 16, 20, 24, 32, 40, 48, 56, 64, 72, and 80 K km s^{-1}. The kinematic distances corresponding to $V_{\rm LSR}$ are also indicated in the bottom of each panel. [*See the electronic edition of the Journal for a color version of this figure.*]

feature is seen at $V_{\rm LSR} \sim -80$ to -70 km s^{-1} (Fig. 2*i*) toward $(l,\ b) = (347.^{\circ}30,\ 0.^{\circ}05)$, which was also suggested to be interacting with the SNR (Slane et al. 1999), although the kinematic distances of cloud A and the -70 km s^{-1} cloud differ by $\sim$3 kpc, making it highly unlikely that both of the clouds are a connected single cloud interacting with the SNR. At $V_{\rm LSR} \sim -60$ to -50 km s^{-1} (Fig. 2*k*), weak CO features appear to surround the SNR in the northwest, while this was not noted before. The panel at $V_{\rm LSR} \sim -50$ to -40 km s^{-1} (Fig. 2*l*) shows little CO emission, and these velocities correspond to the interarm. At $V_{\rm LSR} \sim -40$ to -20 km s^{-1} (Figs. 2*m* and 2*n*) the supershell SG 347.3-0.5-21 mentioned above is seen. This supershell has a significantly larger radius than that of the SNR G347.3$-$0.5, while some of the CO features appear to overlap with the SNR perhaps by chance. What is most remarkable, a panel (Fig. 2*p*) at -10 to -0 km s^{-1} shows that the CO distribution appears to delineate the SNR boundary well. For over three-quarters of the SNR boundary except for the southeast edge, the X-ray image seems to be bound by the CO emission. This is the velocity component ascribed to be interacting with the SNR in Paper I. More details of the features are shown in the following sections (§§ 3.3 and 3.4). We also note that a strong CO peak at $(l,\ b) = (347.^{\circ}1, -0.^{\circ}4)$ in Figure 2*o* is likely associated with the SNR (see § 3.4). Beyond $V_{\rm LSR} \sim 0$ km s^{-1}, the CO emission shows a fairly good

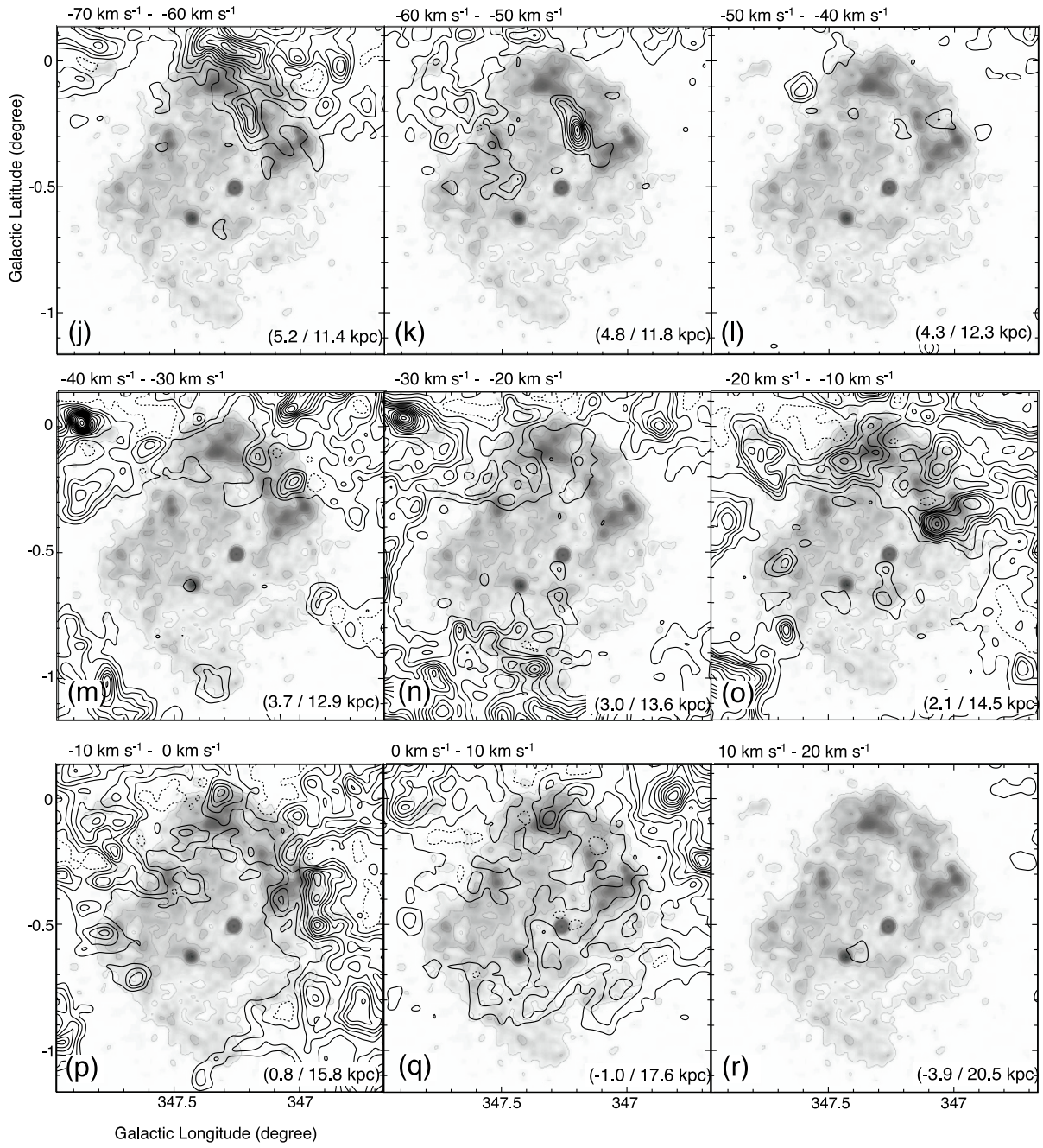

FIG. 2.—*Continued*

correspondence with the depression of the X-ray image toward $l \sim 347.^{\circ}0$–$347.^{\circ}4$ and $b \sim -0.^{\circ}6$ to $-0.^{\circ}7$, which is elongated by half a degree from the southwest to east. This depression is ascribed to the absorption by a local molecular gas at 0–10 km s^{-1} in § 3.6. We note that most of the CO emission seen in Figure 2*q* is due to the local clouds independent of the others at minus velocities. The local clouds have narrow line widths of $\sim$1.5 km s^{-1} and peak velocity of $\sim$6–7 km s^{-1}, clearly distinguished from the distant clouds at $V_{\rm LSR} < 0$ km s^{-1}, as seen in Figure 1*b*.

Figure 1*a* shows that the molecular distribution toward G347.3−0.5 generally shows a depression toward the SNR, and Figure 2 indicates the same trend. Here we introduce a factor to describe the degree of geometrical contact between the CO and X-ray images, which may help one to test how the molecular gas is in contact with the SNR at each distance. This factor, a "covering factor," is defined as the ratio of the covering angle of the CO distribution surrounding the SNR boundary to the whole angle of the SNR in each velocity range every 10 km s^{-1}. We adopt the center of the angular measurement to be $(l,\ b) = (347.^{\circ}3,\ -0.^{\circ}5)$. For simplicity, this covering angle is calculated only for the overlapping region of the SNR boundary and CO lowest contours in the channel maps shown in Figure 2. The contributions from the isolated clouds located inside the X-ray boundary are not included. Figures 3*a* and 3*b* are schematics for estimating the covering factor. The factor is $\sim$10% in the case of Figure 3*a* and 80% in Figure 3*b*.

Since the distribution of molecular clouds toward G347.3−0.5 generally tends to surround the SNR and to avoid the interior region of the SNR in any velocity range, except for the positive velocity corresponding to the local cloud components, the covering factor gives a quantitative measure of the overall spatial coincidence between CO and X-rays around the boundary of the

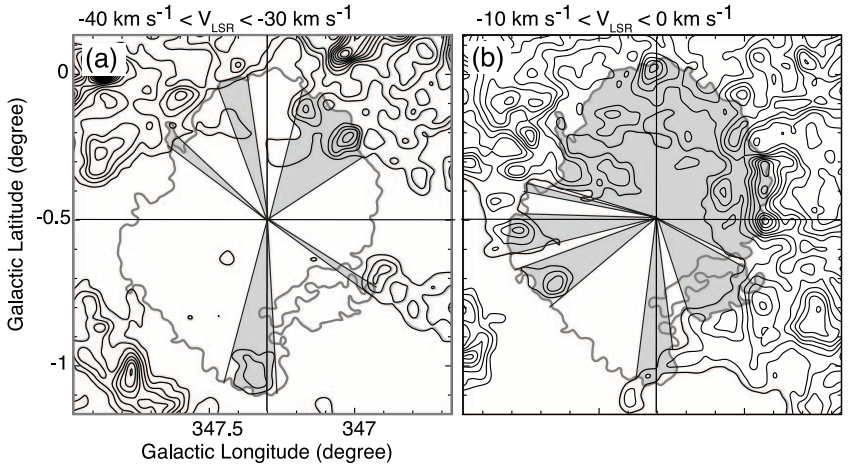

FIG. 3.—Pair of ^{12}CO ($J = 1–0$) velocity channel maps (*black contours*) superposed with the *ROSAT* X-ray boundary line of the SNR (*gray contours*). The velocity ranges are (*a*) from −40 to −30 km s^{-1} and (*b*) from −10 km s^{-1} to 0 km s^{-1}. The minimum contour level and the contour interval of CO are 4 K km s^{-1}. The covering angles (*gray colored regions*; see text) are measured from (l, b) = (347.°3, −0.°5).

SNR. The covering factor is shown as a function of V_{LSR} in Figure 4. For most velocity ranges, the factor is less than ∼40%, but at around −10 km s^{-1} it becomes largest, ∼80%, indicating that the correlation of CO with the SNR is the highest at that velocity range in Figure 2*p*. We suggest that this lends additional support to the assignment of the low-velocity CO emission as interacting with the SNR in Paper I.

3.3. *Detailed Comparisons with X-Rays*

In order to make a more detailed examination of the spatial correlation between the X-ray features and the interacting molecular gas at the velocity range from ∼−20 to ∼0 km s^{-1}, we show in Figure 5 a superposition of the *ROSAT* image for the whole SNR and CO and in Figure 6 a superposition of the *XMM-Newton* image at a harder energy range (2–7 keV) and at higher angular resolution (15″; Hiraga et al. 2005). Figure 5*a* shows the gray-scale and contour map of ^{12}CO ($J = 1–0$) integrated intensity, and Figure 5*b* shows a superposition of the *ROSAT* X-ray image at an energy range of 0.1–2.0 keV on the CO for a velocity range from −12 to −3 km s^{-1}, which as we find shows the best correlation with the SNR.

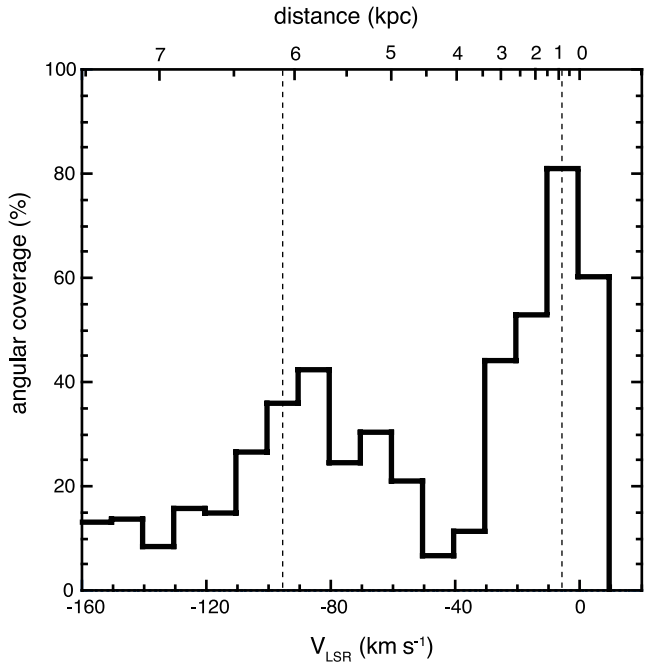

FIG. 4.—Histogram of the angular coverage of CO distribution surrounding the boundary of the SNR. The covering factor is defined as a fraction of the angle summed up, where the CO distribution is overlapped by the outer boundary of the X-ray SNR. The mean central position of the X-ray–emitting area is taken as (l, b) = (347.°3, −0.°5), and for each velocity bin of 10 km s^{-1}, the CO boundary is defined as the lowest contour level in each channel map of Fig. 2. The kinematic distance scale corresponding to V_{LSR} is also indicated in the top of each panel, and the assumed distances of G347.3−0.5 (1 kpc/6 kpc) are denoted by dashed lines.

In order to estimate the physical parameters of the molecular gas interacting with the SNR, we need to identify molecular clouds. As shown in Figures 5 and 6, we named CO peaks from A through Y, while we admit that the complicated CO distribution makes it difficult to identify clouds uniquely. A, B, C, and D have been used in Paper I, and in addition to these, we indicate other peaks of weaker intensity as E through Y. Basic physical properties of the clouds tentatively identified are listed in Table 1. We note that the present cloud definition does not have significant influence on later discussion of the physical aspects of the interaction.

The method of defining a CO cloud is as follows:

1. In Figure 5, an area enclosed by the contour of 8.5 K km s^{-1} (equal to 5 σ level for the integration for a velocity range of 8 km s^{-1}), which is significantly above the extended emission, is defined as an individual cloud.
2. For the case in which a CO peak has relatively weak intensity (≤6.5 K km s^{-1}), the area enclosed by the contour of 4.5 K km s^{-1} is identified as an individual cloud (O, Q, R, S, T, U, and V).
3. For a cloud for which it is hard to define a closed boundary with the contour of 8.5 K (because the area enclosed by the contour is too small or extended filamentarily), a circular area with a radius of 4′, slightly larger than the beam size, around the peak position is defined as the size of the cloud for simplicity (F, I, H, K1, and K2).
4. When a peak position is separated by 0.°3 or larger from the nearest boundary of the *ROSAT* X-ray image in Figure 5*b*, the cloud is regarded as not associated directly with the SNR and is not taken into account [e.g., (l, b) ∼ (346.°73, 0.°02), (347.°71, 0.°10)].
5. When a CO spectrum has a double-peaked profile, each velocity component is defined as an independent cloud in the case for which the velocity difference between the two peaks is larger

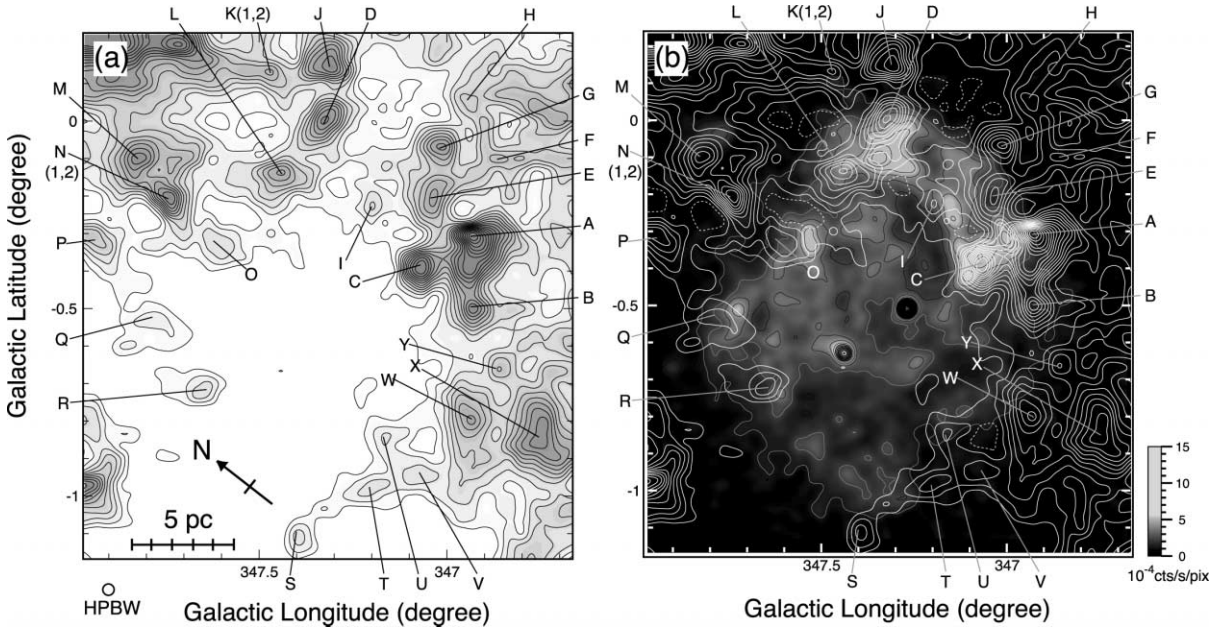

FIG. 5.—(*a*) Intensity distribution of ^{12}CO ($J = 1$–0) emission. The intensity is derived by integrating the ^{12}CO ($J = 1$–0) spectra from −12 to −3 km s^{-1}. The lowest contour level and interval are 2.5 K km s^{-1}. The CO peaks A–Y discussed in § 3.3 are indicated in the figure. (*b*) Overlay map in Galactic coordinates showing G347.3−0.5 X-ray image in gray scale (from *ROSAT* archive database) and ^{12}CO ($J = 1$–0) distribution in white contours. The contour levels and the velocity range of the CO map are the same as in (*a*). [*See the electronic edition of the Journal for a color version of this figure.*]

than 5 km s^{-1}, ∼2.5 times larger than the typical line width of a cloud (K1, K2, N1, and N2). The two components are divided at the velocity of the intensity minimum between the peaks.

6. When two or more peaks are contained in one area enclosed by a contour, the areas divided at the minimum in the intensity map are defined as independent peaks.

In Figure 5, the stronger CO peaks tend to be located close to the X-ray intensity peaks on the west and northwest. The most prominent X-ray peaks at (l, b) = (347.°1, −0.°3) and (347.°3, −0.°05) are well correlated with CO peaks; X-ray peak (347.°1, −0.°3) is associated with peaks A and C. B is not obvious here, but as shown later, B is associated with an X-ray peak at a harder energy band. The X-ray peak at (347.°3, −0.°05) is associated with D and L, where D is coincident with the CANGAROO and HESS TeV γ-ray peak (Paper I; Aharonian et al. 2004). Most of these CO peaks, including E and G, are located just on the outer edge of the SNR, as is consistent with a picture that the SNR

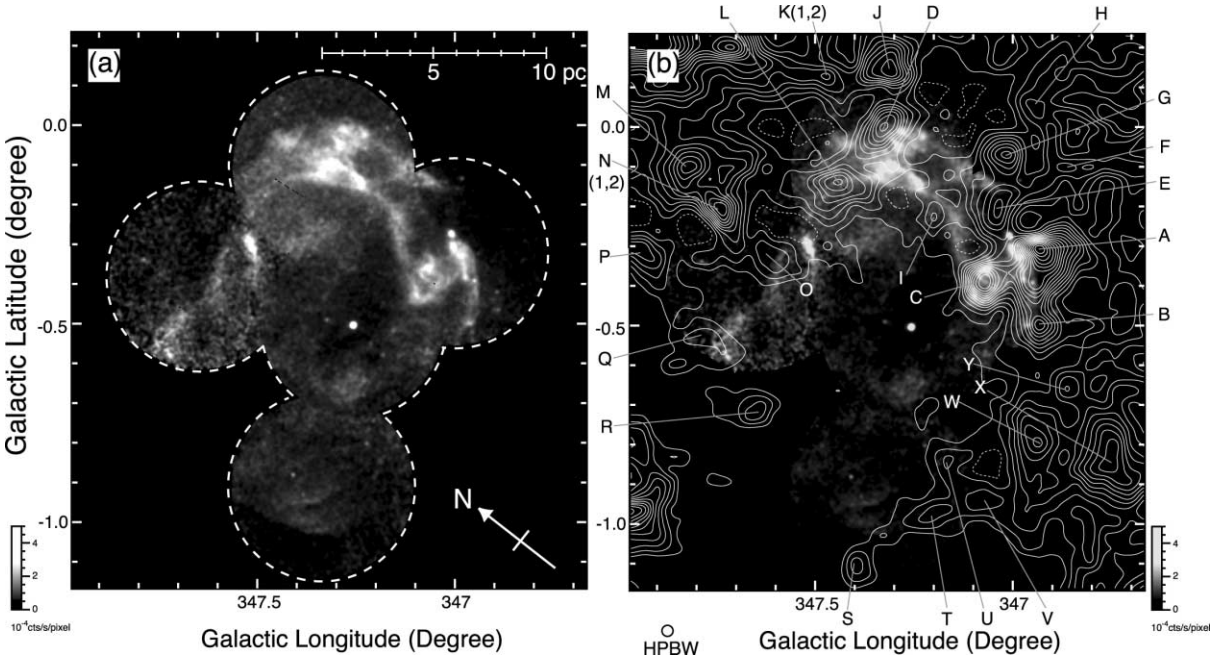

FIG. 6.—(*a*) X-ray image of G347.3−0.5 taken by *XMM-Newton* (Hiraga et al. 2005) in gray scale. An observed area is indicated with dashed lines. (*b*) Overlay map of G347.3−0.5 *XMM-Newton* image in (*a*) and ^{12}CO ($J = 1$–0) intensity contours. The CO contours and the velocity range are the same as those in Fig. 5. The depressions of the CO emission with the lowest contour level inside of the molecular boundary are shown with dashed contours to avoid confusion. The CO peaks A–Y discussed in § 3.3 are indicated. [*See the electronic edition of the Journal for a color version of this figure.*]

TABLE 1
PROPERTIES OF ^{12}CO ($J = 1-0$) CLOUDS

Name (1)	l (deg) (2)	b (deg) (3)	T_R^* (K) (4)	V_{peak} (km s^{-1}) (5)	ΔV_{LSR} (km s^{-1}) (6)	Size (pc) (7)	L_{CO} (10^2 K km s^{-1} pc^2) (8)	Mass ($M_\odot$) (9)	Comment (10)
A	346.933	−0.300	8.5	−10.3	4.8	4.2	32.5	686	Peak A
B	346.933	−0.500	4.2	−8.0	4.6	2.1	9.0	190	Peak B
C	347.067	−0.400	9.4	−12.0	3.8	3.0	18.8	397	Peak C
D	347.300	0.000	4.0	−10.1	4.8	3.0	13.9	292	Peak D
E	347.033	−0.200	2.0	−6.1	7.2	3.0	7.5	159	
F	346.867	−0.100	2.3	−3.5	5.0	2.7	6.2	131	
G	347.033	−0.067	3.3	−10.8	8.0	2.7	14.6	307	
H	346.933	0.033	1.5	−6.5/−8.5	–	2.4	5.1	109	
I	347.200	−0.233	1.8	−9.9	5.4	2.4	4.9	103	
J	347.300	0.133	5.5	−11.3	3.4	3.0	15.5	326	
K1	347.467	0.133	1.2	−4.3	3.6	2.7	2.3	48	
K2	347.467	0.133	2.2	−11.0	4.8	2.7	7.6	160	
L	347.433	−0.133	4.0	−12.0	5.7	3.0	17.6	370	
M	347.867	−0.100	2.0	−9.5	6.3	3.3	14.8	312	
N1	347.767	−0.200	1.5	−4.0	4.0	2.4	8.5	178	
N2	347.767	−0.200	2.7	−10.9	6.1	2.4	3.9	83	
O	347.600	−0.333	1.1	−6.4	4.9	2.4	2.9	61	
P	347.933	−0.333	1.4	−8.3	9.0	2.7	6.7	141	
Q	347.800	−0.533	2.9	−2.8	3.2	3.0	5.1	108	
R	347.667	−0.733	4.1	−3.3	2.4	2.7	3.2	67	
S	347.400	−1.133	3.3	−4.8	1.5	1.8	1.8	38	
T	347.200	−0.967	3.3	−4.7	2.1	2.7	2.9	62	
U	347.167	−0.833	3.7	−4.8	1.3	2.4	2.7	58	
V	347.067	−0.933	3.6	−4.3	2.2	2.4	2.7	57	
W	346.933	−0.800	5.0	−5.1	3.0	4.0	19.0	402	
X	346.733	−0.867	5.7	−5.6	3.4	4.2	27.8	586	
Y	346.867	−0.667	3.4	−4.5	3.0	1.8	4.2	88	

NOTES.—Col. (1): Cloud name. Cols. (2)–(3): Position of the observed point with the maximum ^{12}CO ($J = 1-0$) intensity peak. Cols. (4)–(6): Observed properties of the ^{12}CO ($J = 1-0$) spectra obtained at the peak positions of the CO clouds. Col. (4): Peak radiation temperature T_R^*. Col. (5): V_{LSR} derived from a single Gaussian fitting. Col. (6): FWHM line width ΔV_{peak}. Col. (7): Size defined as an effective diameter $=(A/\pi)^{0.5} \times 2$, where A is the total cloud surface area defined as the region surrounded by the contour of 8.5 or 6.5 K (see text). If the contour is unclosed, the boundary is defined as the intensity minimum between the nearby peaks. Col. (8): The CO luminosity of the cloud L_{CO}. Col. (9): Mass of the cloud derived by using the relationship between the molecular hydrogen column density $N(H_2)$ and the ^{12}CO ($J = 1-0$) intensity $W(^{12}CO)$, $N(H_2) = 2.0 \times 10^{20}[W(^{12}CO)/(\mathrm{K\ km\ s^{-1}})]$ (cm^{-2}) (Bertsch et al. 1993). Col. (10): The names of the peaks A–D identified in Paper I are noted.

shock is impacting these molecular clumps from the inside out. We also note that peaks O, Q, and R correspond to the X-ray peaks at $(l, b) = (347.^\circ52, -0.^\circ30)$, $(347.^\circ72, -0.^\circ50)$, and $(347.^\circ60, -0.^\circ73)$, respectively. In the south, the molecular gas including CO peaks S–Y also delineates the SNR boundary well. To summarize, at scales of arcminutes, the X-ray image shows a good spatial correlation with the NANTEN CO image.

Figure 6 shows an even more striking correspondence between CO and X-rays at $10''$ scales taken with *XMM-Newton* at an energy range harder than that in Figure 5. This X-ray image should be less affected by foreground absorption than the *ROSAT* image. The CO peaks A and B are well delineated by the thin X-ray filament, which becomes clear in this harder energy range, extending by $15'$ in the northwest-southeast. This thin filament is not well traced in Figure 5, perhaps due to the absorption effect in the southeastern half of the filament facing CO peak B and also in part due to the lower resolution of *ROSAT*. Peak C appears surrounded by two thin X-ray features of a few to several arcminute lengths in the northwest and southeast. Peak D is also X-ray–bright in the south. The other peaks are all located just outside the X-ray features. The inside of the SNR around the point source (1WGA J1713.4−3949) is almost empty in the CO distribution. To summarize, this comparison further confirms the remarkable spatial correlation seen in Figure 5 at a finer angular resolution by a factor of 3.

3.4. *Submillimeter Results;* CO *($J = 3-2$) Emission*

Three regions of probable sites of the interaction, ^{12}CO ($J = 1-0$) peaks A, C, and D, have been mapped in the ^{12}CO ($J = 3-2$) emission with ASTE. The same transition has also been observed toward peak C with the CSO 10.4 m telescope. The intensity distributions of the CO ($J = 3-2$) emission toward peaks A, C, and D are shown in Figure 7. The ratios of the integrated intensities of the $J = 3-2$ and $J = 1-0$ emission are $\sim$0.7, $\sim$0.8, and $\sim$0.5 toward peaks A, C, and D, respectively, where each CO intensity has been integrated within a contour at half-intensity levels (11 σ, 8 σ, and 6 σ level in the $J = 3-2$ distribution, respectively). We also note that the $J = 3-2$ line is generally not sufficiently excited to be observable with the current typical sensitivity in most of the cold molecular clouds in the Galaxy; toward peak C, the $J = 3-2$ emission is seen at $V_{LSR} = -11$ and -90 km s^{-1}, only toward two of the four components seen in the $J = 1-0$ emission (Fig. 8).

Here we use the large velocity gradient (LVG) radiative transfer model to obtain constraints on the physical conditions in the molecular gas. The LVG model is a useful method for solving the equations of radiation and collision for molecular excitation states. In the LVG model, it is assumed that the molecular cloud has a velocity gradient and that all photons radiated in the cloud escape without absorption because a different

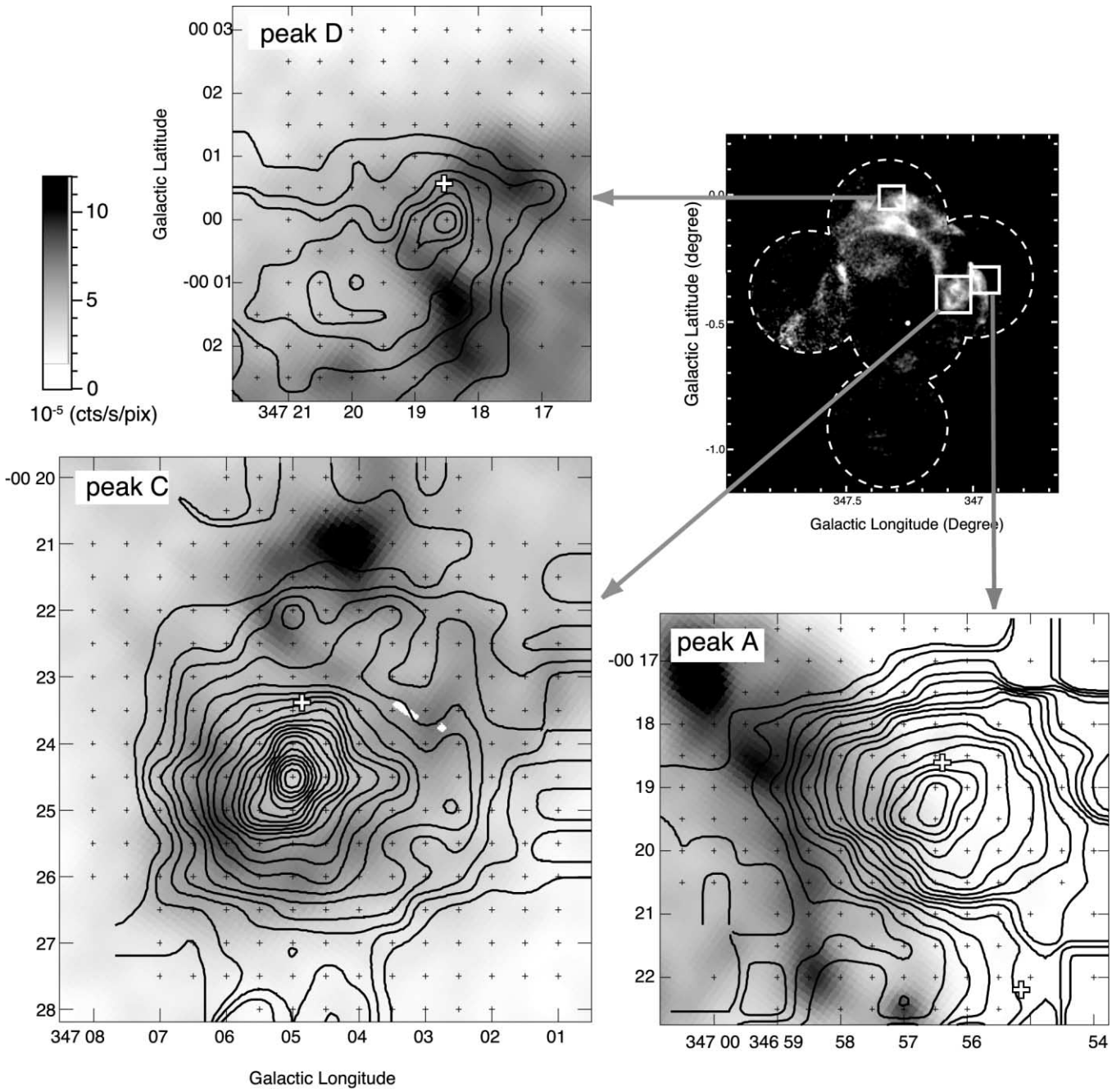

FIG. 7.—Distribution of CO ($J = 3-2$) emission obtained with the ASTE submillimeter telescope (*contours*) superposed with the *XMM-Newton* X-ray image (*gray scale*). The beam size of the ASTE was 23″. The three regions including CO peaks A, C, and D are shown with an insert of the *XMM-Newton* image on the top right. The velocity range is from -12 to -3 km s^{-1} in peaks A and C and from -12 to -8 km s^{-1} in peak D. The CO contours are every 1.5 K km s^{-1} from 3.0 K km s^{-1} in peak C and peak D and every 1.5 K km s^{-1} from 6.0 K km s^{-1} in peak A. Observed positions are indicated by crosses. Open crosses show the positions of the *IRAS* point sources in each panel (see Table 3). The white boxes in the X-ray image at $(l,\ b) = (347^{\circ}03',\ -00^{\circ}23.'5)$ are due to the absence of data.

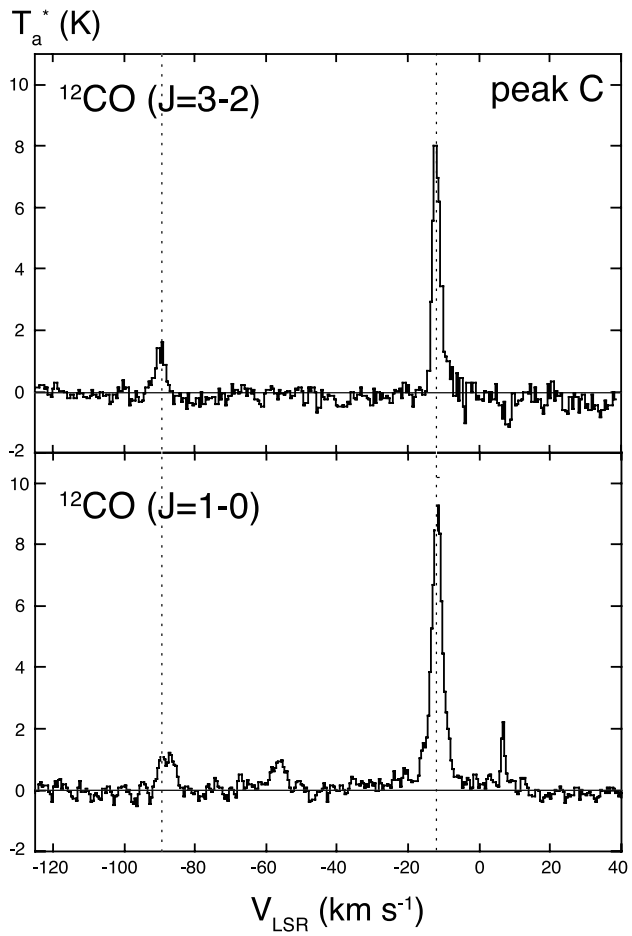

FIG. 8.—*Top:* ^{12}CO ($J = 3-2$) spectrum at (l, b) = (347.°100, −0.°400) covering both the −11 km s^{-1} component and the −90 km s^{-1} one, taken by CSO. *Bottom:* ^{12}CO ($J = 1-0$) spectrum taken with NANTEN at (l, b) = (347.°100, −0.°367). The peak velocities of the −11 and −90 km s^{-1} components are denoted by dashed lines.

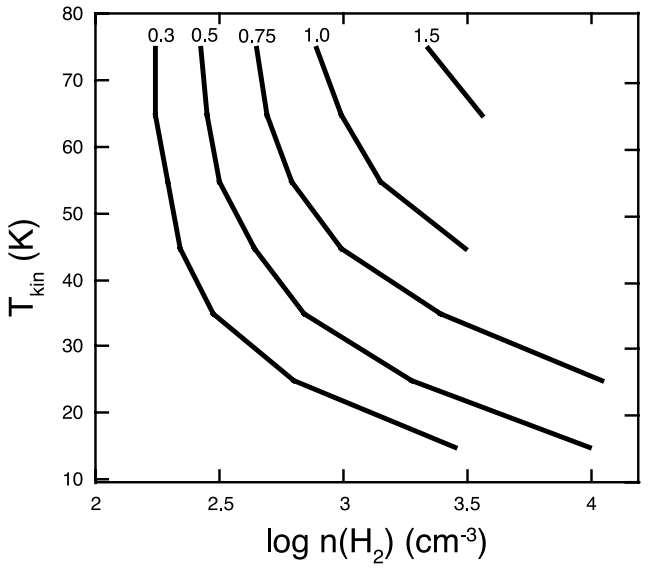

FIG. 9.—Results of LVG calculations for $X(\mathrm{CO})/V = 10^{-4.5}$ pc km^{-1} s. The calculations are carried out for values of $T_{\rm kin}$ from 15 to 75 K with an interval of 10 K. Solid lines indicate constant values of $T_R^*(J = 3-2)/T_R^*(J = 1-0) = 0.3$, 0.5, 0.75, 1.0, and 1.5.

position has a different Doppler velocity shift. In this analysis, we use a LVG calculation method developed by Kim et al. (2002) based on Goldreich & Kwan (1974). In the model, the radiative transfer equation gives the population of each excitation state as a function of the kinetic temperature of the gas, $T_{\rm kin}$, for the molecular hydrogen number density $n(\mathrm{H_2})$. For each observed point of CO ($J = 3-2$) and ($J = 1-0$), we invert these functions to determine the $T_{\rm kin}$ and $n(\mathrm{H_2})$ corresponding to the observed line ratios (see Fig. 9). The model assumes a plane-parallel cloud geometry. The parameter needed for the model is the ratio $X(\mathrm{CO})/V$, where $X(\mathrm{CO})$ is the fractional CO abundance and V is the velocity gradient. We adopt $X(\mathrm{CO})/V = 10^{-4.5}$ pc km^{-1} s in this case.

With the LVG analysis, we find that peaks A and C require rather high density and temperature as listed in Table 2. The lowest temperature for peak A must exceed 30 K if we adopt a typical density less than $\sim 10^3$ cm^{-3}; we note that the typical density and temperature in local ^{12}CO-emitting dark clouds are 10^3 cm^{-3} and 10 K, respectively (e.g., Snell 1981). This indicates that the high-J transition of CO is appreciably excited in peaks A and C and that the gas is warm, being consistent with the shocked molecular gas (e.g., Arikawa et al. 1999; Irwin & Avery 1992; Zhu et al. 2003). In particular, peak A showing the good correlation with the X-ray–bright filament requires a higher temperature than in typical quiescent molecular gas in the solar vicinity. In the excitation conditions of typical cold molecular gas in nearby dark clouds with low-mass star formation [$T_{\rm kin} \sim$ 10–20 K, $n(\mathrm{H_2}) \sim 10^3$–$10^4$ cm^{-3}], the $J = 3-2$ transition is only weakly excited and the line intensity ratio between the $J = 3-2$ and $J = 1-0$ lines is likely below 0.3, significantly less than what is observed in the three peaks of G347.3−0.5 (see Fig. 9). Unfortunately, the observational data in the CO ($J = 3-2$) emission is quite limited over the Galaxy and only a limited number of areas have been observed so far (e.g., Hunter et al. 1997; Yamaguchi et al. 2003). In order to make an estimate of the general CO $J = 3-2/J = 1-0$ ratio in typical molecular clouds in the solar vicinity that are not subject to extreme excitation conditions, here we integrate the CO emission of the present $J = 3-2$ data and NANTEN $J = 1-0$ data of the three regions toward G347.3−0.5 (shown in Fig. 7) by eliminating the regions of probable interaction in velocity space. The results are as follows: the $J = 3-2/J = 1-0$ ratios are $<$4.2 K km s^{-1}/ 130 K km s^{-1} = 0.03 in the local clouds in $V_{\rm LSR} = 0$–10 km s^{-1} (4.2 K km s^{-1} corresponds to a 3 σ detection limit of $J = 3-2$ emission over the integrated velocity range) and 23 K km s^{-1}/ 91 K km s^{-1} = 0.25 in the Sagittarius arm ($V_{\rm LSR}$ from −35 to −20 km s^{-1}). Thus, the ratio is below 0.3 in the other quiescent regions as is consistent with the above estimate for the nearby dark clouds.

We therefore infer that the present high ratios of 0.7–0.8, in particular, between the $J = 3-2$ and $J = 1-0$ lines in G347.3−0.5 lend support to highly excited states that are rather uncommon among the Galactic molecular gas, keeping in mind that a more extensive survey in the CO $J = 3-2$ emission over the Galactic molecular gas is highly desirable to better establish this in the future. This temperature rise is perhaps due to local enhanced heating by the SNR, for which possible mechanisms may include X-rays, γ-rays, and/or cosmic-ray protons. We postpone dealing with more details about the heating mechanisms until the possible contribution by another young source becomes reasonably well understood (see below).

In order to test an alternative possibility for explaining the higher temperature, we looked for embedded infrared sources toward the CO peaks in the *IRAS* (*Infrared Astronomical Satellite*)

TABLE 2
RESULTS OF LVG ANALYSIS AT MOLECULAR PEAKS

Name (1)	l (deg) (2)	b (deg) (3)	$T_{CO(J=1-0)}$ (K) (4)	$T_{CO(J=3-2)}$ (K) (5)	$R(3-2/1-0)$ (6)	$T_{kin}(n = 10^3/n = 10^4)$ (K) (7)
Peak A.....	346.94	−0.32	8.9	7.5	0.8	50/30
Peak C.....	347.08	−0.40	9.3	6.5	0.7	40/25
Peak D.....	347.30	0.00	4.2	2.0	0.5	30/14

NOTES.—Col. (1): Cloud name. Cols. (2)–(3): Position of the ^{12}CO ($J = 3-2$) intensity peak. Col. (4): Peak radiation temperature T_R^* of ^{12}CO ($J = 1-0$) emission. Col. (5): Peak radiation temperature T_R^* of ^{12}CO ($J = 3-2$) emission averaged in the region within a contour at half-intensity levels for comparison with that of $J = 1-0$. Col. (6): Ratio of $T_{CO}(J = 3-2)$ to $T_{CO}(J = 1-0)$ considering dilution effect of $J = 1-0$ beam. Col. (7): Kinetic temperature assuming $n(H_2) = 10^3$ cm^{-3} (*left*) and $n(H_2) = 10^4$ cm^{-3} (*right*).

Point Source Catalog (1988). It turns out that all three regions are associated with *IRAS* sources as listed in Table 3 (see also peaks A, C, and D in Fig. 7) and all of them appear to have steeply rising far-infrared spectra explicable as embedded young stars. It is not certain whether all these are really at the same distance as the molecular peaks, 1 kpc, and the physical association needs to be more carefully checked. If we tentatively assume that they are at 1 kpc, their radiation luminosities are estimated as 140–560 $L_\odot$, which may contribute to heating up the molecular gas to some degree. Thus, we postpone affirming the shock heating/compression in the two peaks A and C until better estimates of density and temperature become available and until the association of the *IRAS* sources is better established.

In conclusion, the strong submillimeter emission of CO shown in this work certainly demonstrates highly excited conditions of the molecular gas interacting with the SNR, while it remains open whether the conditions should be solely ascribed to the shock interaction or whether an additional heating may be caused by young stars that are embedded. Further efforts to better constrain the physical parameters of the molecular gas and the nature of the *IRAS* sources are essential.

3.5. *Broad Wings*

Observations made by both ASTE and CSO indicate that peak C shows fairly strong CO $J = 3-2$ emission with some winglike feature. The CO $J = 1-0$ wings had already been discovered and are discussed in terms of the shock acceleration by the blast wave in Paper I. It is possible that the submillimeter wings indicate the accelerated gas due to the interaction with the SNR.

Figure 10 shows a CO $J = 1-0$ profile map of the peak C region. The broad wings have ~20 km s^{-1} extent, showing a peak at −11 km s^{-1}, and are localized within 2′–4′ (~0.6–1.2 pc at 1 kpc). The blueshifted component is seen from ~−23 to −14.5 km s^{-1}, and the possible redshifted component from ~−9.0 to −7 km s^{-1}. For the redshifted side, we note that confusion with the other clouds at V_{LSR} from ~−6 to 0 km s^{-1} makes it difficult to separate the wing component clearly. There also remains a possibility that the $J = 1-0$ redshifted winglike profile is not due to the shock acceleration but just a superposition of unshocked clouds.

As shown in Figure 11, a CO $J = 3-2$ profile map, peak C exhibits broad wings. These submillimeter wings are more intense in the blueshifted side and are more localized than $J = 1-0$ wings within ~0.3 pc of the intensity maximum of peak C. In Paper I, it is argued that the CO broad wings in peak C may represent the accelerated molecular gas due to the impacting blast wave of the SNR. For the blueshifted wing, we confirm that this is a viable interpretation since the higher density/temperature of the wings indicated by the submillimeter spectrum is consistent with this interpretation.

The present wings are seen in both the red- and blueshifted sides of the quiescent gas. Such a trend is not odd in shocked gas and is seen in the other shock-excited cases (e.g., IC 443, van Dishoeck et al. 1993; W28, Arikawa et al. 1999). These two velocity components may be due to complicated geometry of the shock fronts; a possibility here is that the far and near sides of peak C are being shocked to produce the two components. It is also remarkable that the size of the $J = 3-2$ wing is much smaller than that of the $J = 1-0$ wings. This suggests that the higher excitation condition in density is localized toward the central part of peak C.

Here we should note an alternative possibility that the wings may represent molecular outflow driven by young protostars (for molecular outflows see, e.g., Lada 1985; Fukui et al. 1986, 1989, 1993). The above-mentioned *IRAS* source IRAS 17089−3951 toward peak C (Table 3) may lend support to this alternative. The total molecular mass of peak C is estimated to be ~400 $M_\odot$ by assuming the X-factor for ^{12}CO ($J = 1-0$), 2×10^{20} cm^{-2} K^{-1} (km s^{-1})$^{-1}$ (Bertsch et al. 1993), and the luminosity of the *IRAS* source ~300 $L_\odot$ seems consistent with a young stellar object embedded in it. By assuming that it is a protostellar molecular outflow, the physical quantities, kinetic

TABLE 3
IRAS POINT SOURCES TOWARD MOLECULAR PEAKS

IRAS Name (1)	l (deg) (2)	b (deg) (3)	F_{12} (Jy) (4)	F_{25} (Jy) (5)	F_{60} (Jy) (6)	F_{100} (Jy) (7)	L_{IRAS} ($L_\odot$) (8)	Comment (9)
17082−3955	346.94	−0.31	5.4	3.8	17.5	138	137	Peak A
17089−3951	347.08	−0.39	4.4	13.0	98.5	234	311	Peak C
17079−3926	347.31	0.01	2.0	20.0	88.6	739	562	Peak D

NOTES.—Col. (1): *IRAS* source name. Cols. (2)–(3): Position of the source. Cols. (4)–(7): Fluxes of 12, 25, 60, and 100 μm bands, respectively. Col. (8): *IRAS* luminosity estimated using formula of Emerson (1988). Col. (9): Nearby ^{12}CO ($J = 3-2$) peak (see text).

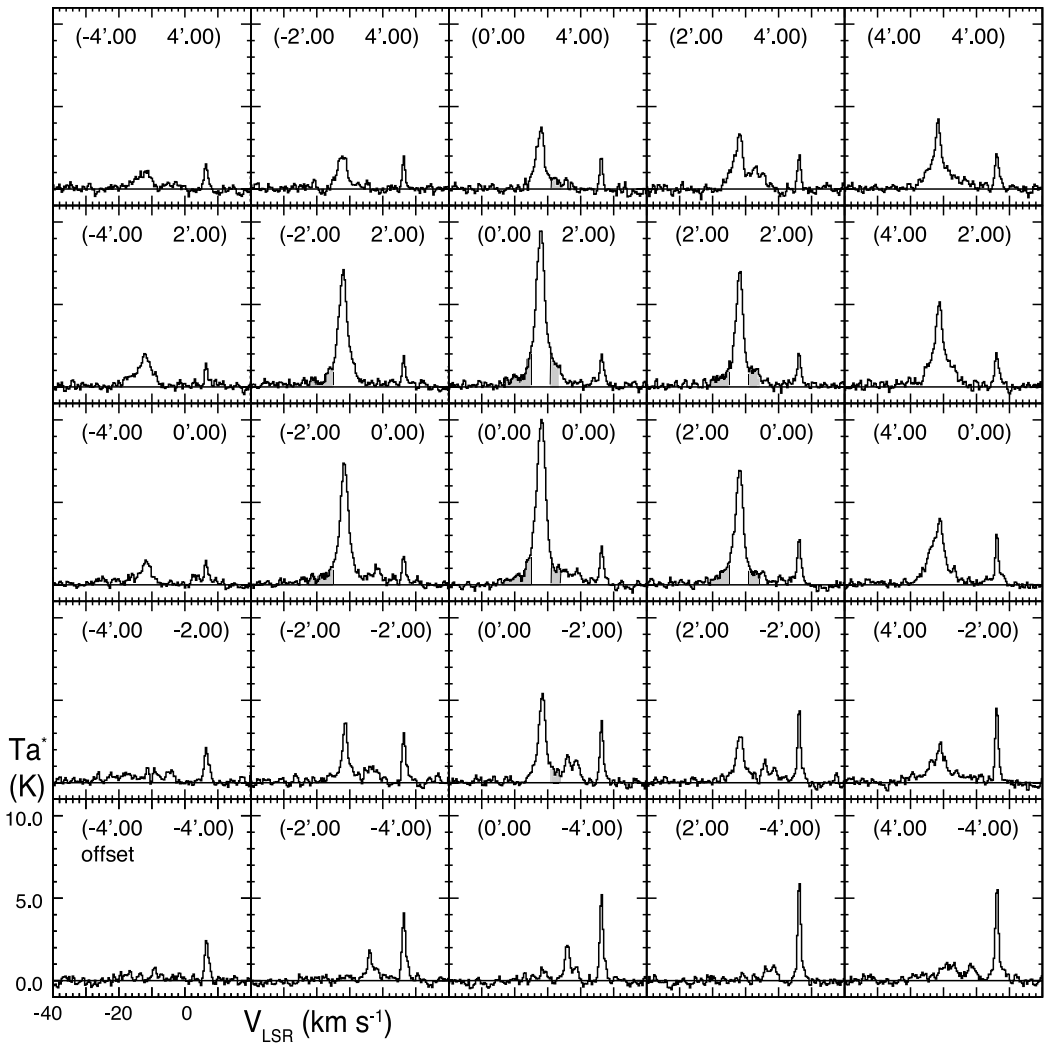

FIG. 10.—Profile map of ^{12}CO ($J = 1-0$) spectra toward peak C. The central position is (l, b) = (347.°07, −0.°40), and the offset for each position is 2′ in Galactic coordinates. The offset values in arcminutes are denoted in each panel. The velocity range is from −40 to 20 km s^{-1}. The wing components are indicated by gray colored areas.

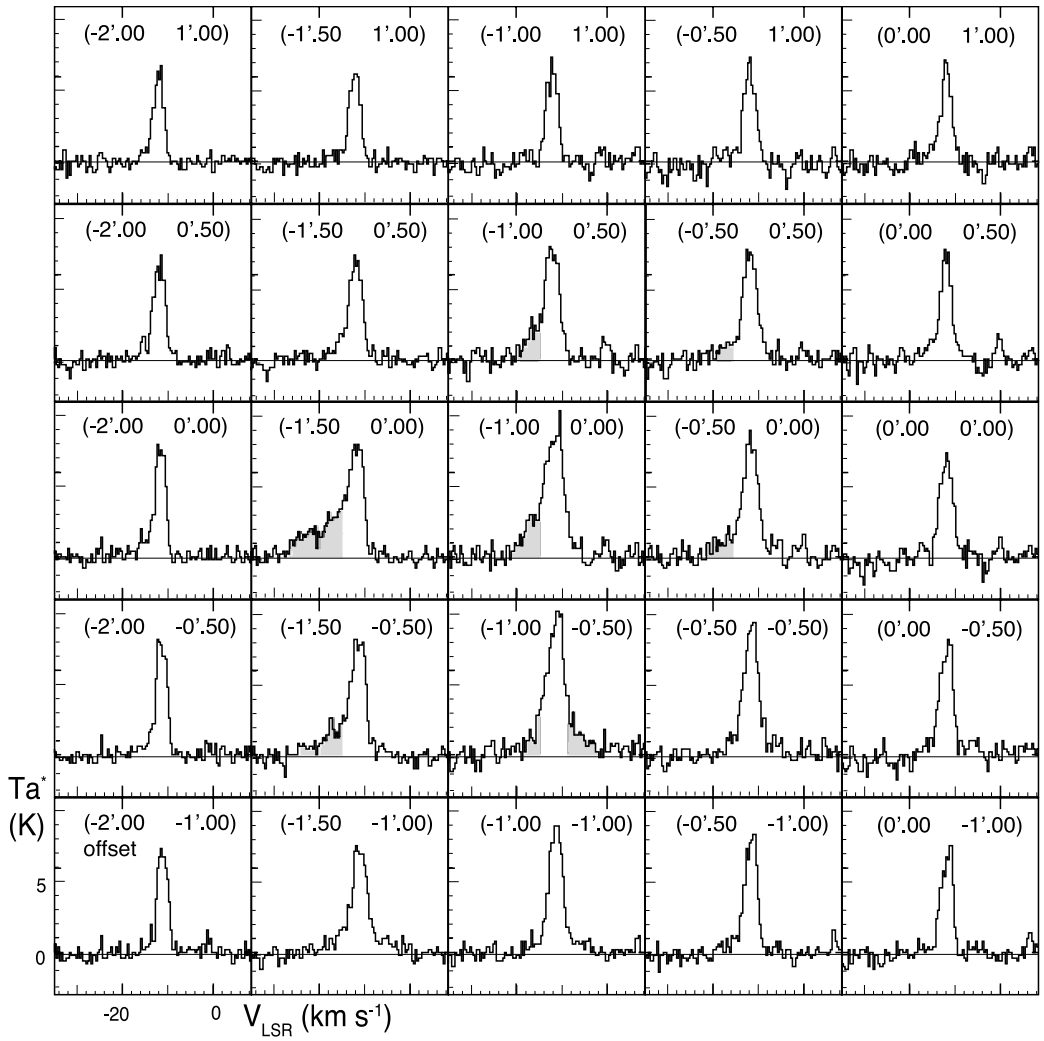

FIG. 11.—Profile map of ^{12}CO ($J = 3-2$) spectra toward peak C. The central position is (l, b) = (347°.08, −0°.400), and the offset for each position is 0′.5 in Galactic coordinates. The offset values in arcminutes are denoted in each panel. The velocity range is from −35 to 8 km s^{-1}. The wing components are indicated by gray colored areas.

TABLE 4
^{12}CO ($J = 1-0$) Outflow Properties

Property	Blue	Red
Integrated intensity (K km s^{-1})	21.5	8.7
Mass ($M_\odot$)	18	7
Size (arcmin)	4.5	3.7
Size (pc)	1.3	1.1
ΔV (km s^{-1})	9.0	9.0
P ($M_\odot$ km s^{-1})	162	63
$E_{\rm kin}$ (10^{45} ergs)	15	6
$t_{\rm dyn}$ (10^5 yr)	1.5	1.2
$L_{\rm mech}$ ($L_\odot$)	1.8	0.8
$F_{\rm CO}$ (10^{-3} $M_\odot$ km s^{-1} yr^{-1})	1.1	0.5

Notes.—The total intensity is estimated integrating over the area enclosed by a contour of 2.0 K for the integrated velocity range of -25 km s^{-1} $\le V_{\rm LSR} \le -16$ km s^{-1} for the blueshifted component and -8 km s^{-1} $\le V_{\rm LSR} \le -6$ km s^{-1} for the redshifted component. Size is defined as an effective diameter $=(A/\pi)^{0.5} \times 2$, where A is the region enclosed by a contour of 2.0 K. Mass is derived by using the relationship between the molecular hydrogen column density $N(\rm H_2)$ and the ^{12}CO ($J = 1-0$) intensity $W(^{12}{\rm CO})$, $N(\rm H_2) = 2.0 \times 10^{20}[W(^{12}{\rm CO})/({\rm K\ km\ s^{-1}})]$ (cm^{-2}) (Bertsch et al. 1993). The quantity ΔV is a velocity range of the wing component estimated from the blueshifted lobe (for redshifted, the same value as that for blueshifted is adopted tentatively). The quantities P (momentum), $E_{\rm kin}$ (kinematic energy), $t_{\rm dyn}$ (dynamical age), $L_{\rm mech}$ (mechanical luminosity), and $F_{\rm CO}$ (CO momentum flux) are defined as mass $\times\Delta V$, $1/2M\Delta V^2$, size/ΔV, $1/2M\Delta V^3/R$, and $P/t_{\rm dyn}$, respectively.

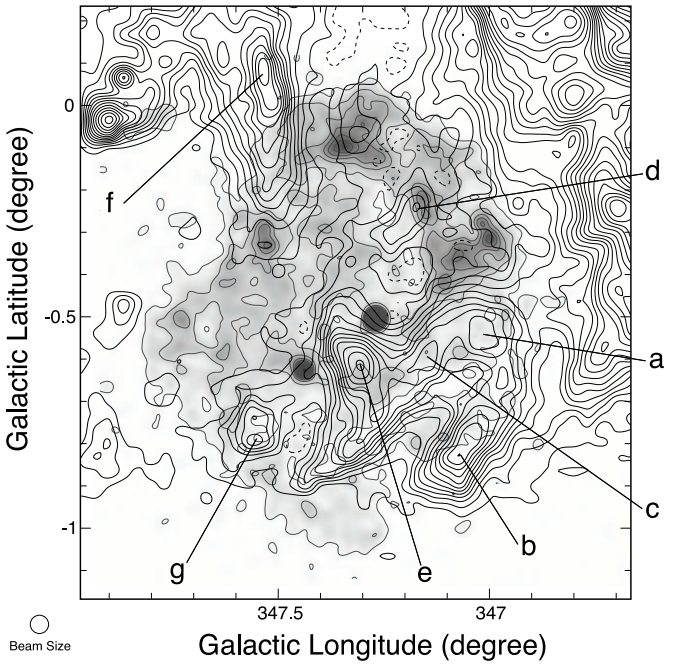

Fig. 12.—CO intensity map integrated in the velocity range from 6.5 to 7.5 km s^{-1} superposed with the same *ROSAT* X-ray image as in Fig. 2 in gray scale. The positions of the local intensity peaks are denoted by (*a*)–(*g*). The lowest contour level and interval are 0.7 and 0.5 K km s^{-1}, respectively. The depressions of the CO emission with the lowest contour level inside of the molecular boundary are shown with dashed contours to avoid confusion. [*See the electronic edition of the Journal for a color version of this figure.*]

energy, momentum, and mass of outflow are estimated (Table 4) and it seems that these quantities are not unreasonably different from typical parameters of outflow (Fukui et al. 1989; 1993).

If this interpretation is correct, peak C may represent a preexisting dense star-forming cloud core that happened to be close to the SN, and the enhanced density in it may have allowed the core to survive against the blast wave. The possibility of the protostellar outflow in peak C should be further pursued by mid-infrared imaging and spectroscopy of the *IRAS* source, as well as by higher resolution molecular observations.

In summary, we confirm the CO broad wings in peak C in both the $J = 1-0$ and $J = 3-2$ CO transitions and present two alternative interpretations; one is the shock acceleration by the SNR blast waves as in Paper I, and the other is the molecular outflow driven by a protostar. We need to accumulate more observations to discriminate between these alternatives.

3.6. *Local Cloud Absorption*

The previous comparison of the 0–10 km s^{-1} velocity window (Fig. 2*q*) suggests that absorption of soft X-rays may be affecting the appearance of the X-ray distribution. Generally speaking, the southern region of the SNR is relatively weak in X-rays, suggesting possible absorption; a most notable soft X-ray depression in the *ROSAT* image is a straight feature extending from (l, b) $\sim$ (347.°0, $-0.°7$) to (347.°4, $-0.°9$) over half a degree, which may be due to absorption. In the following, we make a detailed comparison of CO with soft X-rays and show that the soft X-ray image may be considerably affected by the foreground absorption by molecular gas.

Figure 12 is for comparison with the molecular clouds in a velocity range from 6.5 to 7.5 km s^{-1} that is probably responsible for the absorption of X-rays. The main component of the molecular clouds is located in the southern part of the SNR, from $l = 346.°9$ to 347.°4 and from $b = -0.°4$ to $-1.°0$. Including this, we have named seven CO peaks from *a* through *g* as listed in Table 5.

We list the likely candidates for absorption below.

1. The main cloud including peaks *a*, *b*, *c*, and *e* corresponds to the weaker X-ray intensity. In particular, we note that the most intense X-ray arc in the northwest toward the southwest appears bound by the main cloud at (l, b) $\sim$ (347.°05, $-0.°45$). This suggests that the sharp cutoff of the X-ray arc may be due to absorption at least in part.

2. The straight X-ray depression feature from (l, b) $\sim$ (347.°0, $-0.°5$) to (347.°4, $-0.°9$) corresponds well to the CO ridge in the same direction.

3. A few CO peaks are also located toward the regions of weaker X-ray intensity: *f* at (l, b) $\sim$ (347.°55, $-0.°2$ to $+0.°2$) and *g* at (l, b) $\sim$ (347.°55, $-0.°75$). The exception is *d* at (l, b) = (347.°20, $-0.°25$), where a weak CO peak is overlapped by part of the northwestern X-ray rim.

These are promising candidates for absorption features and could be more firmly established through detailed spectral analysis in the X-ray energy spectra. The CO integrated intensities of these peaks are 6.0–12.6 K km s^{-1}, corresponding to an atomic column density of $\sim(2.8-5.0) \times 10^{21}$ cm^{-2} [an X-factor of 2×10^{20} cm^{-2} K^{-1} (km s^{-1})$^{-1}$ is adopted]. The absorption column density based on the recent X-ray observations (Cassam-Chenai et al. 2004a; Hiraga et al. 2005) is in the range $(4-10) \times 10^{21}$ cm^{-2}, fairly consistent with our results within a factor of $\sim$2. This column density of several $\times 10^{21}$ cm^{-2} is large enough to cause the absorption (e.g., Tatematsu et al. 1990), while the probable variation in the X-ray intensity may make it difficult to estimate the amount of absorption quantitatively. In conclusion, we have shown that the soft X-ray image of G347.3$-$0.5, particularly in the south, is likely affected by the foreground absorption due to the local molecular cloud within several hundred parsecs of the Sun, and any detailed analysis of the soft X-ray distribution is to be made

TABLE 5
PROPERTIES OF LOCAL CLOUD PEAKS

Name (1)	l (deg) (2)	b (deg) (3)	V_{LSR} (km s^{-1}) (4)	T_R^* (K) (5)	ΔV (km s^{-1}) (6)	Integrated Intensity (K km s^{-1}) (7)	$n(H)_{CO}$ (10^{21} cm^{-2}) (8)
a	347.02	−0.54	6.4	9.4	1.3	11.8	4.7
b	347.07	−0.83	7.0	5.7	1.2	6.9	2.8
c	347.15	−0.60	6.7	6.7	1.5	10.1	4.0
d	347.17	−0.24	7.1	2.9	2.1	6.0	2.4
e	347.30	−0.62	7.0	7.3	1.7	12.6	5.0
f	347.53	0.08	7.1	7.7	1.6	11.9	4.8
g	347.55	−0.79	6.3	6.9	1.1	7.7	3.1

NOTES.—Col. (1): Peak name. Cols. (2)–(3): Position of the ^{12}CO ($J = 1$–0) peak. Col. (4): V_{LSR} derived from a single Gaussian fitting. Col. (5): Peak radiation temperature T_R^*. Col. (6): FWHM line width ΔV_{peak}. Col. (7): ^{12}CO ($J = 1$–0) integrated intensity from a single Gaussian fitting. Col. (8): Hydrogen column density estimated from CO intensity assuming an X-factor of 2×10^{20} cm^{-2} K^{-1} (km s^{-1})$^{-1}$ (Bertsch et al. 1993).

by taking this into account. More quantitative study of the absorption toward the molecular clouds is desirable by using new X-ray data sets in the future. We also need to further consider the possible contribution of H I. This is to be done in the future with appropriate high-resolution H I measurements.

Anyway, it is likely that most of these clouds in positive velocity are local components within several hundred parsecs of the Sun. The fact that the clouds can be recognized as dark extinction features in optical pictures (Digitized Sky Survey archive data from ESO/ST-ECF Science Archive) supports this suggestion.

It may be worthy to discuss the origin of the small positive velocities of the local clouds. One of the possible explanations is that these clouds are parts of the Gould belt. The Gould belt passes through the area of $b \sim 0^\circ$–10° at $l \sim 347^\circ$ (Taylor et al. 1987), close to the location of the clouds at issue. Taylor et al. (1987) also estimated the distance and the expansion velocity of the Gould belt ring to be ~300 pc and ~5 km s^{-1} respectively, which are not inconsistent with the properties of these clouds. We can speculate on other explanations for the positive velocities, such as the random motion or the streaming motion of the clouds. Dispersion due to random motion of local clouds is measured on the order of several km s^{-1} (e.g., ~4 km s^{-1} by Liszt et al. 1984; ~8 km s^{-1} by Stark & Brand 1989), and the streaming motion due to the velocity field of the Galactic density wave is estimated to be ~4 km s^{-1} in the solar vicinity (e.g., Burton & Bania 1974). Each of these hypotheses is capable explaining of the positive velocity of ~6–7 km s^{-1} in this case.

4. DISCUSSION

4.1. *Distance*

Based on the good spatial correlation between CO and X-rays, the authors in Paper I argued that the distance of the SNR G347.3−0.5 is most likely 1 kpc instead of the 6 kpc previously favored. The present detailed analysis of the same CO data sets also confirms this small distance.

The peak velocity range of the molecular clouds named A–Y in § 3.3 is −12 to −3 km s^{-1} (Table 1). Most of the clouds are highly likely to be at almost the same distance and associated with the SNR, since they show good spatial coincidences with the X-ray distribution. The velocity centroid of these clouds is ~−6 km s^{-1} as remarked in Paper I, giving the kinematic distance of ~1 kpc. Here we adopt the Galactic rotation curve model by Brand & Blitz (1993) for deriving kinematic distances. If one assumes that the distance of these clouds in the velocity range of −12 to −3 km s^{-1} is uniformly 1 kpc, they are localized in an area of ~20 pc (=1° in angular size) and have a maximum dispersion of the peak velocities of ~9 km s^{-1}. A simple and feasible explanation of this cloud-cloud velocity dispersion is the initial proper motion. Generally, it is not unusual that localized molecular clouds have velocity dispersions of around several to 10 km s^{-1}, being due to random and/or streaming motion. Thus, in this case it is also natural to regard these clouds in the velocity range of −12 to −3 km s^{-1} as having almost the same distance of ~1 kpc.

We note that the range of kinematic distances corresponding to the velocity range of −12 to −3 km s^{-1} is about 0.5–2.0 kpc. However, such an uncertainty does not conflict with our supposition that G347.3−0.5 is basically at the smaller distance.

It is also noteworthy that recent work, independent of Paper I, has provided support for the small distance; these are studies of the X-ray and interstellar absorption (Uchiyama et al. 2003; Koo 2003; Cassam-Chenai et al. 2004a) and HESS TeV γ-ray image (Aharonian et al. 2004). Koo (2003) and Cassam-Chenai et al. (2004a) analyzed the interstellar absorption by using low-resolution H I (15′–30′) and CO (8′) data and concluded that the X-ray absorption is consistent with the small distance ~1 kpc as opposed to the large distance ~6 kpc. Uchiyama et al. (2003) posed a constraint that the shock velocity must be >5000 km s^{-1} from *Chandra* observations of the northwestern shell, implying that G347.3−0.5 is a quite young SNR. The physical properties of the SNR derived assuming the distance of 1 kpc are consistent with this demand for the shock velocity (see next subsection).

The HESS TeV γ-ray image has revealed a detailed distribution of the highest energy photons. Their major finding is a shell-like distribution of TeV γ-rays similar to the X-ray distribution. These authors support the distance of 1 kpc by noting that the TeV γ-ray peaks are stronger in the northwestern region where the interaction between the local molecular gas and the SNR is suggested in Paper I and that the TeV γ-ray flux is weak toward the eastern regions where cloud A was suggested to be interacting. The small distance of 1 kpc is therefore acquiring even stronger support since the publication of Paper I.

4.2. *Evolution of the SNR*

In this section we discuss the evolution of the SNR specifically for the case of 1 kpc distance, which is strongly supported observationally by the present work, as well as by others (e.g., Koo 2003; Cassam-Chenai et al. 2004a; Aharonian et al. 2004). Slane et al. (1999) had already discussed that the two distances, 1 and 6 kpc, are both possible in explaining the evolution of the SNR,

TABLE 6
PHYSICAL PROPERTIES OF G347.3−0.5

Parameter	1 kpc	6 kpc
Diameter (60′)	17.4 pc	104 pc
Historical record	AD 393[a]	...
Age (yr)	1600	>10000
Evolution phase	Free expansion	Sedov
Ambient density (cm^{-3})	<0.01	0.003[b]
Shock velocity (km s^{-1})	5500	3200[b]
Shock temperature (keV)	35	12[b]
Ejecta	Nonradiative	Radiative
Swept-up mass ($M_\odot$)	<3	35[b]
Emission integral (cm^{-5})	$<5 \times 10^{16}$	2×10^{15}[b]
Central source emitting area (km)	3	0.5
Total energy of accelerated particle (ergs)	$\sim 2 \times 10^{49}$	$\sim 10^{50}$

NOTES.—The physical parameters for 1 and 6 kpc distance are shown in this table. The remnant age for 6 kpc is assumed to be 20,000 yr to estimate ambient density, shock velocity, shock temperature, swept-up mass, and emission measure.

[a] Wang et al. (1997).

[b] Assuming 2×10^4 yr of age.

although the timescales, etc., should be quite different between the two cases. Here we highlight the main aspects of the SNR evolution at 1 kpc; we do not intend to use the evolutionary models to discern the distance, since it is no longer required.

There are seven historical supernovae, and G347.3−0.5 likely corresponds to the historical SN AD 393, the only one that has escaped identification among the seven recorded in the historical literature (Wang et al. 1997). Thus, we confirm that G347.3−0.5 corresponds to SN AD 393 and adopt its age as ∼1600 yr.

The small distance 1 kpc drastically changes many physical parameters of the SNR from those expected in the case of 6 kpc. Various physical parameters are compared for the two distances 1 and 6 kpc in Table 6. At 1 kpc, the radius of the SNR is 8.7 pc and the age is as small as ∼1600 yr. Because of a lack of thermal X-ray emission, the emission measure of the X-ray–emitting hot gas should be very small, like $\sim 10^{15}$ cm^{-5} (e.g., Slane et al. 1999). Such a very low emission measure should require very low densities of the postshock region. It also indicates that the total mass of swept-up matter is not large enough to achieve the adiabatic phase and the remnant is still in free-expansion phase with thermal nonequilibrium between electrons and ions. If we assume that the progenitor is a massive star and the ejecta mass is 3 $M_\odot$ (Borkowski et al. 1996), the explosion energy of 10^{51} ergs gives an ejecta velocity of 5800 km. This velocity is nearly equal to the average velocity of the shock front ∼5500 km s^{-1} as derived from X-ray measurements (e.g., Koyama et al. 1997; Uchiyama et al. 2003), indicating that the blast wave has not been decelerated yet. If we apply a simple model that the free expansion phase ends when the swept-up mass becomes equal to the mass of ejecta, we infer that the explosion occurred in low-density surroundings having a density of <0.01 cm^{-3} and that the ejecta is nonradiative at present. We then obtain an emission measure of $\int n_e n_{\rm H}\, dl < 3 \times 10^{15}$ cm^{-5}. This value is nearly the same as that in the case of 6 kpc distance (Table 6) and is small enough to explain the lack of thermal emission. In addition, the electron temperature is estimated to be <0.5 keV by applying the analytic formula developed by Masai (1994) to the X-ray data (Slane et al. 1999). This low value of electron temperature is consistent with the observed X-ray spectrum. We confirm that the basic X-ray properties of the SNR are explained consistently at 1 kpc.

Slane et al. (1999) reported that the spectrum of the central object 1WGA J1713.4−3949 can be fitted with a 0.38 keV blackbody model and the radius of the emitting region is $0.5^{+0.16}_{-0.11}$ times the diameter at 1 kpc. The temperature of the blackbody model is significantly higher than that of a cooling neutron star whose age is ∼1600 yr (e.g., Slane et al. 2002). The polar cap heating model seems to be good in this case and is able to explain the observed temperature and the radius of the emitting region plausibly at 1 kpc. Here we have to note another possibility still remaining that the central object is not associated with the SNR. Slane et al. (1999), for instance, pointed out that the X-ray spectra of the central object can be fitted by either a power-law or thin thermal emission model with absorption having the column density comparable to the total absorption through the Galaxy in this direction. To summarize, the physical parameters are well explained in the framework of a very young SNR in the free expansion phase at 1 kpc. Another detailed discussion of the SNR evolution can be found elsewhere (e.g., Cassam-Chenai et al. 2004a).

4.3. *Origin of Gamma Rays and Cosmic-Ray Protons*

Higher quality multiwavelength data including radio, X-rays, and γ-rays are needed to obtain definitive conclusions on cosmic-ray acceleration in G347.3−0.5, the most unique object known to date in testing the proton acceleration. Higher energy X-ray imaging observations will provide synchrotron cutoff energy, and more sensitive X-ray spectroscopy is needed to detect thermal X-ray emission. Gamma-ray observations with higher spatial resolution will allow us to better constrain the acceleration mechanism.

It is in this context a very important issue to understand precisely the mechanism of TeV γ-ray emission in G347.3−0.5. For this purpose, it is essential to discern the contributions of the cosmic-ray proton component from the electronic contribution via inverse Compton process, and this should be achieved by making a detailed comparison between spatially resolved images of CO and TeV γ-rays.

The recent HESS image of TeV γ-rays (Aharonian et al. 2004) is certainly encouraging in that it is beginning to resolve the TeV-γ distribution at a few arcminutes, similar to the angular resolution of the NANTEN CO data set. It is particularly intriguing that the TeV γ-ray distribution largely resembles that of the CO distribution in that they are enhanced in the northwestern rim of the SNR as noted by Aharonian et al. (2004). While the statistical significance in HESS results may not yet be high enough to make a detailed comparison of the individual peaks, we make a preliminary estimate of the efficiency for proton acceleration over the entire SNR by using a formula from Enomoto et al. (2002), $(E/10^{48})(M_{\rm cloud}/200)(l/3)^{-3}(d/1)^{-5} = 1.35$, where E (ergs) is the total energy of cosmic-ray protons, $M_{\rm cloud}$ ($M_\odot$) the molecular cloud mass interacting with them, l (pc) the typical length of the cloud, and d (kpc) the distance, the same as that in Paper I. We assume that the interacting molecular cloud mass amounts to ∼2500 $M_\odot$ by summing up the major CO peaks in contact with the SNR (from Table 1). The equation gives the total energy of cosmic-ray protons of $\sim 2.4 \times 10^{49}$ ergs, and then the efficiency of the proton acceleration is estimated to be ∼0.024 by dividing by the total energy of the SN explosion, $\sim 10^{51}$ ergs.

5. CONCLUSIONS

We conclude the main results of the present work as follows:

1. The present detailed analysis of the NANTEN CO data has established that the SNR G347.3−0.5 is interacting with the molecular gas at a distance of 1 kpc instead of the 6 kpc previously

suggested. This is supported by subsequent H I and TeV γ-ray studies. The physical picture of the SNR evolution is shown to be consistent with the distance 1 kpc if the SNR is in the free expansion phase.

2. The intense CO $J = 3$–2 emission has been detected toward two of the CO peaks, strongly indicating that the interacting molecular gas is in highly excited states in density and temperature unusual in typical local dark clouds. This provides additional support for the interaction.

3. We note an alternative possibility that *IRAS* point sources, candidates for embedded young stars in the CO peaks, may provide additional heating in these CO peaks, although their actual association needs to be tested by further observations in the infrared and others.

4. Peak C showing strong interaction with the SNR blast wave is established to exhibit broad CO wings in the $J = 1$–0 and 3–2 transitions. Two alternative interpretations for the wings are presented; one is the shock acceleration (Paper I) and the other protostellar outflow. Further observational efforts are desirable to distinguish between them.

5. It is demonstrated that the southern part of the SNR may suffer from significant absorption by a foreground molecular gas within several hundred parsecs, while a quantitative estimate for the absorption is not available at present.

We would like to thank all the staff members of the NANTEN project. We also acknowledge Tadayuki Takahashi, Yasunobu Uchiyama, and Hiraga Junko for their helpful comments. We appreciate the hospitality of all the people of Las Campanas Observatory of the Carnegie Institution of Washington, and we thank Tom Phillips for kindly allocating the observing time of the CSO. The authors greatly acknowledge the hospitality of all members of NAOJ, University of Tokyo, and Osaka Prefecture University who are working for the ASTE project for their dedicated support. The NANTEN project was based on mutual agreements between Nagoya University and the Carnegie Institution of Washington. We also acknowledge that the NANTEN project was realized by contributions from many Japanese public donors and companies.

This research was financially supported by JSPS Grant-in-Aid for Scientific Research (B) 14403001 and MEXT Grant-in-Aid for Scientific Research on Priority Areas 15071202.

REFERENCES

Aharonian, F. A., et al. 2004, Nature, 432, 75
Arikawa, Y., Tatematsu, K., Sekimoto, Y., & Takahashi, T. 1999, PASJ, 51, L7
Bertsch, D. L., Dame, T. M., Fichtel, C. E., Hunter, S. D., Sreekumar, P., Stacy, J. G., & Thaddeus, P. 1993, ApJ, 416, 587
Borkowski, K., Szymkowiak, A. E., Blondin, J. M., & Sarazin, C. L. 1996, ApJ, 466, 866
Brand, J., & Blitz, L. 1993, A&A, 275, 67
Burton, W. B., & Bania, T. M. 1974, A&A, 34, 75
Butt, Y. M., Torres, D. F., Combi, J. A., Dame, T., & Romero, G. E. 2001, ApJ, 562, L167
Butt, Y. M., Torres, D. F., Romero, G. E., Dame, T. M., & Combi, J. A. 2002, Nature, 418, 499
Cassam-Chenai, G., Decourchelle, A., Ballet, J., Hwang, U., Hughes, J., & Petre, R. 2004a, A&A, 414, 545
Cassam-Chenai, G., Decourchelle, A., Ballet, J., Sauvageot, J.-L., & Dubner, G. 2004b, in IAU Symp. 218, Young Neutron Stars and Their Environments, ed. F. Camilo & B. M. Gaensler (San Francisco: ASP), 73
Ellison, D. C., Slane, P., & Gaensler, B. M. 2001, ApJ, 563, 191
Emerson, J. P. 1988, in Formation and Evolution of Low Mass Stars, ed. A. K. Dupree & M. T. V. T. Lago (NATO ASI Ser. C, 241; Dordrecht: Kluwer), 193
Enomoto, R., et al. 2002, Nature, 416, 823
Ezawa, H., Kawabe, R., Kohno, K., & Yamamoto, S. 2004, Proc. SPIE, 5489, 763
Fukui, Y., Iwata, T., Mizuno, A., Bally, J., & Lane, A. P. 1993, in Protostars and Planets III, ed. E. H. Levy & J. I. Lunine (Tucson: Univ. Arizona Press), 603
Fukui, Y., Iwata, T., Mizuno, A., Ogawa, H., & Takaba, H. 1989, Nature, 342, 161
Fukui, Y., Sugitani, K., Takaba, H., Iwata, T., Mizuno, A., Ogawa, H., & Kawabata, K. 1986, ApJ, 311, L85
Fukui, Y., et al. 2003, PASJ, 55, L61 (Paper I)
Ginzburg, V. L. 1957, Prog. Elementary Part. Cosmic Ray Phys., 4, 339
Goldreich, P., & Kwan, J. 1974, ApJ, 189, 441
Hayakawa, S. 1956, Prog. Theor. Phys., 15, 111
Hiraga, J., Uchiyama, Y., Takahashi, T., & Aharonian, F. A. 2005, A&A, 431, 953
Hunter, T. R., Phillips, T. G., & Menten, K. M. 1997, ApJ, 478, 283
Irwin, J. A., & Avery, L. W. 1992, ApJ, 388, 328
Joint *IRAS* Science Working Group. 1988, *IRAS* Point Source Catalog, Ver. 2 (NASA RP-1190; Washington: NASA), http://vizier.u-strasbg.fr
Kim, S., Martin, C. L., Stark, A. A., & Lane, A. P. 2002, ApJ, 580, 896
Koo, B.-C. 2003, in ASP Conf. Ser. 289, Proc. IAU 8th Asian-Pacific Regional Meeting, ed. S. Ikeuchi, J. Hearnshaw, & T. Hanawa (San Francisco: ASP), 199
Koo, B.-C., & Heiles, C. 1991, ApJ, 382, 204
Koo, B.-C., Kang, J.-H., & McClure-Griffiths, N. M. 2004, J. Korean Astron. Soc., 37, 61
Koyama, K., Kinugasa, K., Matsuzaki, K., Nishiuchi, M., Sugizaki, M., Torii, K., Yamauchi, S., & Aschenbach, B. 1997, PASJ, 49, L7
Koyama, K., Petre, R., Gotthelf, E. V., Hwang, U., Matsuura, M., Ozaki, M., & Holt, S. S. 1995, Nature, 378, 255
Lada, C. J. 1985, ARA&A, 23, 267
Lazendic, J. S., Slane, P. O., Gaensler, B. M., Reynolds, S. P., Plucinsky, P. P., & Hughes, J. P. 2004, ApJ, 602, 271
Liszt, H. S., Burton, W. B., & Xiang, D.-L. 1984, A&A, 140, 303
Masai, K. 1994, ApJ, 437, 770
Matsunaga, K., Mizuno, N., Moriguchi, Y., Onishi, T., Mizuno, A., & Fukui, Y. 2001, PASJ, 53, 1003
Muraishi, H., et al. 2000, A&A, 354, L57
Ogawa, H., Mizuno, A., Hoko, H., Ishikawa, H., & Fukui, Y. 1990, Int. J. Infrared Millimeter Waves, 11, 717
Pannuti, T. G., Allen, G. E., Houck, J. C., & Sturner, S. J. 2003, ApJ, 593, 377
Pfeffermann, E., & Aschenbach, B. 1996, in Proc. Röntgenstrahlung from the Universe, ed. H. H. Zimmermann, J. Trümper, & H. Yorke (MPE Rep. 263; Garching: MPE), 267
Reimer, O., & Pohl, M. 2002, A&A, 390, L43
Rho, J., Petre, R., Schlegel, E. M., & Hester, J. J. 1994, ApJ, 430, 757
Seta, M., et al. 1998, ApJ, 505, 286
Shklovskii, I. S. 1953, Dokl. Akad. Nauk SSSR, 91, 475 (Libr. Congr. transl. RT-1495)
Slane, P., Gaensler, B. M., Dame, T. M., Hughes, J. P., Plucinsky, P. P., & Green, A. 1999, ApJ, 525, 357
Slane, P., Hughes, J. P., Edgar, R. J., Plucinsky, P. P., Miyata, E., Tsunemi, H., & Aschenbach, B. 2001, ApJ, 548, 814
Slane, P. O., Helfand, D. J., & Murray, S. S. 2002, ApJ, 571, L45
Snell, R. L. 1981, ApJS, 45, 121
Stark, A. A., & Brand, J. 1989, ApJ, 339, 763
Tatematsu, K., Fukui, Y., Iwata, T., Seward, F. D., & Nakano, M. 1990, ApJ, 351, 157
Taylor, D. K., Dickman, R. L., & Scoville, N. Z. 1987, ApJ, 315, 104
Uchiyama, Y., Aharonian, F. A., & Takahashi, T. 2003, A&A, 400, 567
van Dishoeck, E. F., Jansen, D. J., & Phillips, T. G. 1993, A&A, 279, 541
Wang, Z.-R., Qu, Q.-Y., & Chen, Y. 1997, A&A, 318, L59
White, G. J., Rainey, R., Hayashi, S. S., & Kaifu, N. 1987, A&A, 173, 337
Yamaguchi, N., et al. 2003, in IAU Symp. 221, Star Formation at High Angular Resolution, ed. M. G. Burton, R. Jayawardhana, & T. L. Bourke (San Francisco: ASP), 236
Zhu, M., Seaquist, E. R., & Kuno, N. 2003, ApJ, 588, 243